3D test simulations of the outer radiation belt electron dynamics including electron-chorus resonant interactions

Athina Varotsou [1], Daniel Boscher [2], Sebastien Bourdarie [2], Richard B. Horne [3], Nigel P. Meredith [3], Sarah A. Glauert [3], Reiner H. Friedel [1]

(1) Space Science and Applications, Los Alamos National Laboratory,
Los Alamos, NM, USA,
(2) Office National d'Etudes et Recherches Aérospatiales, Toulouse, France,
(3) British Antarctic Survey, Natural Environment Research Council, Cambridge, UK

athina@lanl.gov, daniel.boscher@oncert.fr, sebastien.bourdarie@onecert.fr, RH@bas.ac.uk, nmer@bas.ac.uk, sagl@bas.ac.uk, friedel@lanl.gov

Abstract

We present results from our 3D simulations using the Salammbô electron radiation belt physical model. We have run steady state and dynamic storm test-case simulations to study the effect of electron-chorus resonant interactions on the radiation belt electron dynamics. When electron-chorus interactions are introduced in the code outside the plasmasphere, results show that a seed population with a kappa distribution and a characteristic energy of 2 keV is accelerated up to a few MeV in the outer radiation belt. MeV electron fluxes increase by an order of magnitude during high magnetic activity conditions especially near L^*~5 and for equatorial mirroring particles. We have also performed a parametric study of various important parameters to investigate how our results could be influenced by the uncertainty that characterizes their values. Results of this study show that if we consider higher values of the radial diffusion coefficients, different initial states and different boundary conditions, we always observe a peak in the L*-profile of the MeV electrons when electron-chorus interactions are included.

1. Introduction

Since the discovery of the radiation belts in 1958 [*Van Allen et al.*, 1958], a lot of progress has been made in understanding and describing the Earth's radiation environment. Scientific and operational satellite data combined with physical simulations have provided a great insight into the dynamics of the charged particle population and the physical processes involved.

One of the most important remaining questions is the definition of the physical processes responsible for the loss and acceleration of relativistic radiation belt electrons. During conditions of high geomagnetic activity these processes are enhanced causing the observed high variability of high energy electrons especially in the outer radiation belt. Relativistic electron fluxes will decrease if losses dominate, but if sources dominate, relativistic electron fluxes will increase, as is observed in approximately half of all moderate and intense geomagnetic storms [*Reeves at al.*, 2003]. The electron variation can be of several orders of magnitude on timescales from hours to days.

Several processes have been proposed to be responsible for the electron energization to MeV energies [e.g., *Friedel et al.*, 2002; *Horne*, 2002]. Radial diffusion was identified from the beginning as one of the most important [*Falthammar*, 1965, 1966]. Charged particles are transported inwards (towards the Earth) across magnetic field lines due to magnetic and electric field variations. Due to the conservation of the first adiabatic invariant (the particle's magnetic moment) particles moving towards regions of stronger magnetic field become more energetic. For equatorial particles the relationship between the energy of the particle and L- the distance (in Earth radii) of a magnetic field line from the center of the Earth at the equator [*McIlwain*, 1961]- is given by:

$$E_1\left(E_1 + 2E_0\right) * L_1^{\,3} = E_2\left(E_2 + 2E_0\right) * L_2^{\,3} \qquad (1)$$

where E_1 and L_1 are the initial energy and distance (from the center of the Earth, in Earth radii) of the particle and E_2 and L_2 are the final energy and distance of the particle. E_0 is the rest energy of the electron which is equal to 0.511 MeV. In addition, enhanced ULF wave activity in the outer electron radiation belt has been associated with enhanced radial diffusion during high magnetic activity conditions [*O'Brien et al.*, 2001; *Elkington et al.*, 1999].

However, numerous recent studies have shown that radial diffusion alone cannot explain all the temporal and spatial flux variations observed [*Reeves et al.*, 1998; *Brautigam and Albert*, 2000; *Obara et al.*, 2000; *Miyoshi et al.*, 2003; *Horne et al.*, 2003b; *Green and Kivelson*, 2004; *Horne et al.*, 2005; *Chen et al.*, 2006; *Fox et al.*, 2006; *Iles et al.*, 2006; *Miyoshi et al.*, 2006; *Shprits et al.*, 2006c; *Chen et al.*, 2007]. *Brautigam and Albert* [2000] studied the October 9, 1991 storm using CRRES data. When they tried to reproduce the measured fluxes with a simple radial diffusion physical model their results underestimated relativistic electron fluxes around L = 4-4.5 and the flux increase during the recovery phase was not well represented by the model. From the data analysis they also observed outward radial diffusion from L = 4-5 during the recovery phase. The same storm was selected by *Horne et al.* [2003b] who studied the electron pitch angle distribution and found it to be energy dependent.

Miyoshi et al. [2006] used the 4D relativistic RAM electron model [*Jordanova et al.*, 1996, 2003; *Jordanova and Miyoshi*, 2005] to simulate the energetic electron dynamics

74 during the October 2001 storm. Their results showed that radial diffusion, the only
75 mechanism included in the model for relativistic energies (E>300 keV), was not
76 sufficient to reproduce the observations. They concluded that an additional mechanism is
77 needed to explain high energy electron enhancements during the storm's recovery phase.
78 *Reeves et al.* [1998], studied the global response of relativistic radiation belt electrons
79 to the January 1997 magnetic cloud using data from LANL geosynchronous, GOES,
80 GPS, POLAR, SAMPEX and HEO and showed that fluxes increased first near $L = 4$ and
81 then at geosynchronous orbit, at $L = 6.6$.
82 *Green and Kivelson* [2004] in their study using POLAR data showed phase space
83 density expressed data as a function of L^* and time for off-equatorial MeV electrons
84 where a local peak appears near $L^* = 4\text{-}5$ during the recovery phase. Similar phase space
85 density profiles were found by *Chen et al.* [2006, 2007] at the equator from combining
86 POLAR, LANL geosynchronous and GPS data. Developing peaks in the electron phase
87 space density were also found in the region $4 < L^* < 5.5$ during relativistic electron flux
88 enhancements observed by the CRRES satellite [*Iles et al.*, 2006].
89 All the above results indicate that radial diffusion is not the only mechanism acting on
90 radiation belt electrons in the outer belt and that a local source is acting which dominates
91 other processes in the $L = 4\text{-}5$ region.
92 Many theoretical, observational and modeling studies have shown that the most
93 probable mechanism acting locally as a high energy electron source is the resonant
94 interaction of electrons with whistler-mode chorus waves leading to energy diffusion of
95 lower energy particles to higher energy. The in situ wave-particle heating mechanism was
96 theoretically discussed decades ago [*Kennel and Engelmann*, 1966; *Kennel*, 1969; *Lyons*,

97 1974] and agrees well with the scenario first proposed by *Thorne et al.* [1974] of
98 important energy diffusion occurring outside the plasmasphere during active geomagnetic
99 times when whistler-mode waves are present. More recently, *Horne and Thorne* [1998]
100 studied different types of electromagnetic waves present in the magnetosphere to estimate
101 the effect these waves could have on the trapped electron population. Whistler-mode
102 waves in the low density environment outside the plasmasphere were found to be good
103 candidates for electron acceleration to MeV energies from in situ energy diffusion of
104 lower energy particles. Following theoretical studies also demonstrated that cyclotron and
105 Landau resonances with whistler-mode chorus waves were the most probable mechanism
106 to produce local acceleration to MeV energies [*Summers et al.*, 1998; *Horne et al.*, 2003a;
107 *Glauert and Horne*, 2005].
108 Observational evidence for chorus-driven electron acceleration to relativistic energies
109 has been mostly provided by CRRES data studies where both particle and plasma wave
110 data were provided [*Meredith et al.*, 2002a,b, 2003a]. *Meredith et al.* [2003a] studied 26
111 geomagnetically disturbed periods and clearly showed the correlation between high levels
112 of lower-band chorus activity and relativistic electron enhancements in the outer radiation
113 belt. Similar studies are currently being performed using POLAR particle and wave data
114 [*Kristine Sigsbee*, GEM 2007 poster and personal communication].
115 Apart from theoretical and observational evidence for chorus-driven electron
116 acceleration to MeV energies, recent radiation belt 2D and 3D modeling efforts have
117 focused on this topic also. *Varotsou et al.* [2005] presented the first results from 3D
118 simulations with the Salammbô physical model [*Beutier and Boscher*, 1995; *Bourdarie et*
119 *al.*, 1996] including both radial diffusion and energy diffusion due to electron-chorus

120 resonant interactions. The simulations showed that when electron-chorus resonant
121 interactions are included in the simulation, an initial seed population of electrons with
122 characteristic plasmasheet energy of 5 keV can be locally accelerated to MeV energies in
123 the outer belt near geosynchronous orbit.

124 In a two dimensional study by *Albert and Young* [2005] the diffusion equation was
125 solved for energy and pitch angle diffusion due to chorus waves including the cross
126 diffusion terms. The authors found that at L = 4.5 phase space density was strongly
127 diffusing from 0.2 MeV up to a few MeV in less than a day.

128 Recently, *Li et al.* (2007) used the 2D UCLA radiation belt model, including energy
129 and pitch-angle diffusion at a fixed L value and showed that the net effect of electron-
130 chorus resonant interactions- including both dayside and night side parallel propagating
131 chorus- is the local acceleration of relativistic electrons. The local increase of MeV fluxes
132 during the recovery phase of a simulated storm persisted even after they introduced
133 strong losses due to EMIC waves and plasmaspheric hiss.

134 In this paper we present a more detailed study that follows the first results presented by
135 *Varotsou et al.* [2005]. We use the 3D Salammbô code to test the effect of each process
136 (loss, acceleration, diffusion) on the flux and phase space density (PSD) profiles of
137 relativistic electrons. The goal of our study is to investigate how different physical
138 processes acting on the electrons influence the radiation belt dynamics. The study is
139 performed for idealistic dynamic test-cases by using a physical model. The advantage of
140 using a physical model is that we can 'turn on' or 'turn off' one of these processes to
141 identify its effect on the radiation belt dynamics. We are not trying to reproduce satellite
142 observations during a storm period at this point. More realistic simulations, using the

143 actual *Kp* variation and a boundary condition from geosynchronous measurements and
144 including high latitude chorus and EMIC waves, are being performed and will be
145 presented in a following paper.

146 The outline of the paper is as follows. The Salammbô 3D model for radiation belt
147 electrons is described in Section 2 and in Section 3 the diffusion coefficients for the
148 electron-chorus interactions are presented together with the method we followed to
149 introduce them into the code. The steady state and dynamic simulations are presented in
150 Section 4, followed by a parametric study for several key parameters in Section 5. In
151 Section 6 we discuss the limitations of the present study and our future goals, and in
152 Section 7 we summarize the results and conclusions of our study.

153

154 **2. The Salammbô 3D electron model**

155 The development of the Salammbô 3D code for the Earth's radiation belts started in the
156 1990s at ONERA in Toulouse, France and continues until today [*Beutier and Boscher*,
157 1995; *Beutier et al.*, 1995; *Bourdarie et al.*, 1996; *Vacaresse et al.*, 1999; *Varotsou et al.*,
158 2005; *Maget et al.*, 2007]. There are two versions of the code, one for protons and one for
159 electrons since the physical processes involved are different in each case. *Beutier and*
160 *Boscher* [1995] first presented the electron physical model based on a Fokker-Planck
161 diffusion equation solved in the (M,J,L^*) phase space, where M is the first adiabatic
162 invariant, the particle's magnetic moment, J is the second adiabatic invariant related to
163 the particle's bounce motion and L^* is the Roederer parameter [*Roederer*, 1970], related
164 to the third adiabatic invariant Φ by $\Phi = 2\pi\alpha^2 B_0 / L^*$ (where α is the Earth's mean
165 radius and B_0 is the equatorial magnetic field magnitude at the Earth's surface). Physical

166 processes included were: radial diffusion, frictional processes by Coulomb interactions
167 with plasmaspheric cold electrons, pitch angle diffusion by Coulomb interactions with
168 atoms and molecules of the high atmosphere and pitch angle diffusion by wave-particle
169 resonant interactions inside the plasmasphere. This version of the code was used by
170 *Bourdarie et al.* [1996] in their effort to simulate the dynamics of radiation belt electrons
171 during a magnetic storm.

172 The current version of the Salammbô 3D code solves the Fokker-Planck equation to
173 estimate electron PSD in the (E,y,L^*) space, where E is the particle's kinetic energy, y is
174 the sine of the particle's equatorial pitch angle, α_{eq}, and L^* is the Roederer parameter. The
175 diffusion equation then translates to the following

176

177 $$\frac{\partial f}{\partial t} = L^{*2}\,\frac{\partial}{\partial L^*}\left(\frac{D_{LL}}{L^{*2}}\frac{\partial f}{\partial L^*}\right) + \frac{1}{yT(y)}\frac{\partial}{\partial y}\left(yT(y)D_{yy}\frac{\partial f}{\partial y}\right) + \frac{1}{a}\frac{\partial}{\partial E}\left(aD_{EE}\frac{\partial f}{\partial E}\right)$$

178 $$-\frac{1}{a}\frac{\partial}{\partial E}\left(a\frac{dE}{dt}f\right) \qquad (2)$$

179

180 where the terms on the right hand side express radial diffusion, pitch angle diffusion
181 (where *T(y)* is an auxiliary function occurring in the bounce frequency expression),
182 energy diffusion (where $a = (E+E_0)[E(E+2E_0)]^{1/2}$, E_0 the electron rest energy) and
183 losses due to friction, respectively. Radial diffusion is assumed under constant first and
184 second adiabatic invariants on one grid. Pitch angle diffusion occurs under constant
185 energy and L^* and energy diffusion is considered under constant pitch-angle and L^* on a
186 second grid. Interpolation methods are used between the two grids. We use logarithmic
187 grids in energy and L^* and a uniform grid in pitch angle. No cross diffusion terms are

188 included in the current version of the code. The introduction of cross diffusion terms is a
189 difficult task which is under study and development [*Albert and Young*, 2005]. The
190 magnetic field used in Salammbô is a dipolar, tilted and eccentric field.

191 The physical processes that drive radial, pitch angle and energy diffusion in the
192 Salammbô code are described in Table 1 (see also diagram in Figure 1 of *Maget et al.*,
193 2007). The fourth and fifth columns indicate which calculation and which parameters
194 were used for the definition of the diffusion coefficients. Note here that radial diffusion
195 coefficients are different from the ones used by *Varotsou et al.* [2005].

196 Inside the plasmasphere, particles interact with hiss, VLF transmitters and lightning-
197 generated whistlers. Outside the plasmasphere, particles interact with whistler-mode
198 chorus waves. In this paper we mainly focus on the region outside the plasmapause where
199 both radial diffusion and chorus waves occur (for more details on the plasmasphere and
200 inner belt region refer to *Beutier and Boscher* [1995]).

201 In addition to these diffusive processes, particle energy loss by Coulomb interactions
202 with cold plasmaspheric electrons and bound electrons of atoms and molecules of the
203 high atmosphere are considered. This process is expressed by the frictional term in the
204 diffusion equation (2). However, interactions with the high atmosphere don't have a
205 significant effect on outer radiation belt electron dynamics, so we will not be analyzing
206 this physical process in any detail (for more details see *Beutier and Boscher* [1995]).

207 In the code, the temporal evolution of PSD is determined by the temporal evolution of
208 the coefficients introduced in the diffusion equation (2). Radial diffusion coefficients and
209 pitch angle and energy diffusion coefficients due to chorus interactions outside the
210 plasmasphere are expressed as a function of geomagnetic activity through the *Kp* index

211 which is time dependent. Furthermore, the position of the plasmapause, which separates
212 the regions where plasmaspheric waves and chorus operate, is also *Kp* dependent
213 [*Carpenter and Park*, 1973]. The intensity of plasmaspheric waves is considered to be
214 constant (not activity dependent) in Salammbô (see Discussion section). The expressions
215 used for the diffusion coefficients together with the boundary conditions and our solving
216 scheme of equation (2) will be described in the following Sections.
217
218 **3. Electron – chorus resonant interactions**
219 **3.1 Diffusion coefficients from PADIE**
220 Pitch angle, D_{yy}, and energy diffusion, D_{EE}, coefficients for cyclotron resonant electron
221 - chorus interactions have been estimated from the PADIE code [*Glauert and Horne*,
222 2005]. The calculation is done using the quasi-linear assumption and is fully relativistic.
223 In the calculation, distributions of wave power and wave normal angles are assumed to
224 be Gaussian [e.g. *Lyons*, 1974]. The wave distribution is considered to peak along the
225 magnetic field direction with an angular spread of 30 degrees. Landau and ± 5 cyclotron
226 harmonic resonances are included in the calculation and waves are assumed to be
227 confined near the equator at magnetic latitudes of $-15^0 < \lambda_m < 15^0$. The conditions and
228 parameters used for the calculation are the same as those used by *Varotsou et al.* [2005],
229 presented here in Table 2. These values are based on wave observations from the Plasma
230 Wave Experiment [*Anderson et al*., 1992] on board the CRRES spacecraft [*Glauert and*
231 *Horne*, 2005].
232 Bounce averaged diffusion coefficients D_{yy} and D_{EE} are calculated by the PADIE code
233 as a matrix with a constant wave amplitude of B_w = 100nT for electron plasma frequency

234 to electron cyclotron frequency ratio (*fpe/fce*) values of 1.5, 2.5, 5.0, 7.5 and 10, electron
235 energies of 0.01, 0.03, 0.1, 0.3, 1, and 3 MeV, and L values of 2.5, 3.5, 4.5, 5.5 and 6.5,
236 with a resolution of less than 1 degree equatorial pitch angle. Diffusion coefficients are
237 set to zero for energies $E < 0.01$ MeV and $E > 3$ MeV and for L values $L < 2.5$ and $L >$
238 6.5. For *fpe/fce* < 1.5 and *fpe/fce* > 10 diffusion coefficients are assumed constant and
239 equal to their values for *fpe/fce* = 1.5 and *fpe/fce* = 10, respectively.
240
241 **3.2 Introduction of D_{yy}, D_{EE} in Salammbô**
242 The diffusion coefficients were related to magnetic activity by constructing a statistical
243 wave model where equatorial values ($-15^0 < \lambda_m < 15^0$) of *f*pe/*f*ce and wave intensity B_{wave}^2
244 measured by CRRES were parameterized for $Kp < 2$, $2 \leq Kp \leq 4$ and $Kp \geq 4$ between $L =$
245 1 to 7, with a resolution of 0.1L and 1 hour in *MLT* [*Meredith et al.*, 2003b]. The
246 coefficient values from the matrix given by PADIE were interpolated to energy, pitch
247 angle and L values corresponding to the Salammbô grid and to *fpe/fce* values
248 corresponding to the ones given from the statistical wave model (CRRES data).
249 For a given energy, L, pitch angle and *Kp*, the diffusion coefficients were calculated in
250 each *MLT* bin according to *fpe/fce* and B_{wave}^2. Finally, for introduction in the Salammbô
251 code, we calculated the coefficients' drift average by summing values over all MLT and
252 dividing by the number of MLT bins. Since electron-chorus interactions are most
253 efficient for low *fpe/fce* and high wave intensities [*Meredith et al.*, 2003b], they were
254 only included in the model outside the plasmasphere.
255 An example of the bounce and drift averaged diffusion coefficients is presented in
256 Figure 1 for $L^* = 4.8$. The first column shows the energy diffusion coefficients as a

function of energy and equatorial pitch angle for the three different *Kp* categories and the second column shows the same dependence for the pitch angle diffusion coefficients. Some important conclusions can be drawn from Figure 1: a) both coefficients increase when geomagnetic activity (*Kp*) increases, b) for high energies both coefficients obtain higher values at higher pitch angles, thus acceleration will be more important near the equator and no high energy electron losses due to diffusion in the loss cone (low equatorial pitch angle values) by chorus waves will occur, and c) pitch angle diffusion for the low energy particles near the loss cone will be fast, thus these particles will experience important losses due to the interaction with chorus waves.

4. Test-case simulations

We solve the diffusion equation (2), using an explicit finite difference scheme, in the E, y (=sinα_{eq}), L^* space in a rectangular domain with 25 nodes in each direction (we chose the number of nodes for a fast execution since the time step of our calculations is limited by the Courant-Friedrichs-Lewy condition [*Courant et al.*, 1967]). The simulation domain in Salammbô extends for energies from 0.1 keV to 5 MeV, pitch angles from 2 degrees to 90 degrees (the lower limit for the equatorial pitch angle, under which electrons are lost in the upper atmosphere, is calculated in the model for each L^* shell- it doesn't take values of less than 2^0) and L^* shells from 1 to 8. Since electron-chorus interactions are introduced in the code for energies from 10 keV to 3 MeV and L^* values from outside the plasmapause to 6.5 and since our goal is to test if these interactions can lead to electron acceleration to MeV energies, the domain of interest in this study, on which we will focus, is for $E > 0.5$ MeV and $L^* > 3$.

280 The boundary conditions we impose for the solution of the diffusion equation are the
281 following
282
283 $$f(E_{\min}) = f_{bound}(E_{\min}) \qquad f(E_{\max}) = 0$$
284 $$f(\alpha_{eq\,\min}) = 0 \qquad f(\alpha_{eq\,\max}) = \partial f / \partial \alpha = 0$$
285 $$f(L^*_{\min}) = 0 \qquad f(L^*_{\max}) = f_{bound}(E)$$
286
287 where f_{bound} is the outer boundary condition (only a function of electron energy) we
288 impose at L^* = 8, which constitutes the source of electrons in the simulation. In our
289 current study this condition is constant with time (a time varying boundary is currently
290 being studied and will be presented in a future paper). With the above boundary
291 conditions we consider that: a) the lowest energy PSD- at the outer boundary- stays
292 constant and there is an absence of multi-MeV energies, b) the loss cone is empty and the
293 pitch angle particle distribution at the equator is flat, and c) losses dominate at L^* = 1 and
294 the source at L^* = 8 is constant and given by the f_{bound} boundary condition.
295 The boundary condition at L^* = 8 is defined to be a kappa distribution [*Christon et al.*,
296 1991] given by the formula
297
298 $$f_{bound} = A\left[1 + \frac{E}{kE_0}\right]^{-k-1} \qquad (3)$$
299
300 where we take $A = 10^{35}$ MeV^{-3}s^{-3}, defined by examining a long period of LANL
301 geosynchronous measurements, E_0 = 2 keV (plasmasheet characteristic energy) , defined

by average LANL geosynchronous MPA (Magnetospheric Plasma Analyzer) data [*Joseph Borovsky* private communication 2007] and $k = 5$, based on *Christon et al.* [1988, 1991]. Note here that *Varotsou et al.* [2005] used a kappa distribution with a characteristic energy of 5 keV, considering a higher energy spectrum at the source.

Finally, to help the reader follow the work and results presented in the following Sections we summarize in Table 3 the physical processes involved in radiation belt dynamics outside the plasmasphere in Salammbô, together with the expressions of the coefficients introduced in the diffusion equation (2) and the simulation domain where each process is included. The plasmapause position is defined by the empirical expression $Lpp = 5.6 - 0.46Kp'$ [*Carpenter and Park*, 1973], where Kp' is the highest value of the Kp index during the last 24 hours of the simulation.

4.1. Steady state

First we present the results obtained for a steady state of the radiation belts. There is no dynamics and no time dependence involved here. This permits us to detect the effect electron-chorus interactions have on the radiation belt electrons when we include them in our simulation scheme. In addition, the initial state for the dynamic simulation is defined from the output of this steady state simulation.

In the steady-state simulation, the diffusion equation (2) is solved for $\partial f/\partial t = 0$. The steady state is defined for a certain geomagnetic activity level, i.e., for a given Kp value. When we fix Kp to a constant value, radial diffusion coefficients depend only on L^*, while pitch angle and energy diffusion coefficients depend on energy, pitch angle and L^*, and the plasmapause is fixed to a certain L^* shell.

325 Radiation belts are considered to initially be empty everywhere except at the outer
326 boundary (L^* = 8) where the source is defined by equation (3). After many iterations, the
327 system reaches a steady state and the calculated phase space densities represent the state
328 of the radiation belts after a long period of steady conditions.
329 We run the code for Kp = 1.3 to use the output as an initial state of calm conditions for
330 our dynamic simulation. To investigate the effect of electron-chorus resonant interactions
331 on the electron distribution we performed one simulation including this process and one
332 without it. The results are presented in Figures 2, 3 and 5.
333
334 **4.1.1. PSD variation as a function of L shell**
335 In Figure 2, phase space densities are presented as a function of L^* shell and iteration
336 number for a constant magnetic moment value of M = 2100 MeV/G and for equatorial
337 mirroring particles (α_{eq} = 90 degrees). The plasmapause position is marked with a white
338 line.
339 In these type of plots, energy increases as we move inwards to lower L^* shells. For M =
340 2100 MeV/G, we are studying ~1 MeV electrons at L^* ~ 6 and ~2 MeV electrons at L^* ~
341 4.5. We choose to represent results in a (M, α_{eq}) = constant space instead of a (M, J) =
342 constant space (where J is the second adiabatic invariant) because we want to be able to
343 distinguish between different processes affecting the electron distribution. In addition, α_{eq}
344 = constant is not that different from J = constant.
345 Figure 2(a) shows results when electron-chorus interactions are included in the
346 simulation together with radial diffusion. First, particles are transported inwards (in the
347 initially empty radiation belts) from the outer boundary by radial diffusion and then they

348 are accelerated by chorus waves resulting to the formation of a peak in the PSD
349 distribution at L^* ~ 5-6. Then, phase space density at surrounding L^* shells (lower than 5
350 and higher than 6) increases due to radial diffusion diffusing particles away from the
351 peak. As a result, phase space density increases inside the plasmasphere and outside L^* =
352 6.5, regions where electron-chorus interactions are not considered in the simulation.
353 In contrast, in Figure 2(b), where results with only radial diffusion included in the
354 simulation are shown, there is no peak forming in the PSD distribution in L^* shell.
355 Particles are only diffused inwards forming a flat PSD distribution. The maximum
356 difference in the PSD values between the two steady states is observed at L^* = 5.5 and is
357 equal to two orders of magnitude. These kinds of increases have been observed at
358 geosynchronous and GPS orbits [*Chen et al.*, 2007].
359
360 **4.1.2. PSD variation as a function of equatorial pitch angle**
361 In Figure 3, results from the two simulations (with and without chorus waves) are
362 presented for comparison as a function of equatorial pitch angle for L^* = 5.2 and for E =
363 1.7 MeV. We choose to present results with respect to energy, equatorial pitch angle and
364 L^* values to confirm that introduction of electron-chorus interactions in a 3D particle
365 simulation leads to energy diffusion, i.e., acceleration of electrons to MeV energies.
366 When electron-chorus resonant interactions are introduced in the simulation we observe
367 an increase in the PSD level. This increase is greater for equatorial pitch angles of 50
368 degrees and higher. Flat top pitch angle distributions like this are a signature of chorus
369 wave acceleration and have been observed by the CRRES satellite (*Horne et al.*, 2003b).

The profile of the red curve (when chorus waves are included in the simulation) can be explained if we look at the profile of the energy and pitch angle diffusion coefficients as a function of equatorial pitch angle. Both coefficients are plotted in Figure 4 for the same parameters as in Figure 3. Energy diffusion coefficients obtain maximum and almost steady values for equatorial pitch angles between 60 and 90 degrees. For α_{eq} < 60 degrees, D_{EE} decreases very fast with decreasing pitch angle, becoming one order of magnitude smaller every ~10 degrees. Pitch angle diffusion coefficients are higher in the region of 50-70 degrees. Their role is to diffuse equatorial particles to lower pitch angle values. Thus, PSD values increase for all equatorial pitch angles (red curve in Figure 3).

In general we conclude that the effect of introducing chorus waves in our simulations is most important for equatorial particles, down to a value of α_{eq}~50 degrees. This is related to our initial hypothesis that chorus waves are confined near the equator (see Discussion section).

4.1.3. PSD variation as a function of energy

Finally, in Figure 5, results are presented as a function of energy for L^* = 5.2 and for equatorial particles (α_{eq}=90 degrees). As in the previous figures, results from the simulation with electron-chorus interactions (red curve) and without (blue curve) are compared. When chorus waves are included, energy diffusion- by which lower energy electrons are accelerated to higher energies- becomes very important. Higher energy phase space densities increase significantly, while lower energy (less than 30 keV) phase space densities decrease. As an example, 600 keV and 1.7 MeV electron phase space

densities increase by more than 2 orders of magnitude while ~ 20 keV electron PSD becomes 2 times smaller.

In reality we don't see low energies decreasing while higher ones increase. The decrease of the low energy phase space densities is an artifact of our simulations since we are considering a constant outer source and convection is not included in the simulation. Observations show that times of enhanced chorus activity coincide with times of enhanced injections and substorm activity [*Meredith et al.*, 2001, 2002a, 2003a]. Thus, the low energy source increases during these times.

4.2 Dynamic simulation

During high geomagnetic activity conditions, variations in the trapped electron distribution can be important and in many cases very fast. Modeling these variations requires a good understanding of the physical processes involved in radiation belt- and magnetospheric- dynamics.

Here, the goal is to expand the study on the combined effect of radial diffusion and electron-chorus resonant interactions presented by *Varotsou et al.* [2005]. We have simulated a simple test-case where *Kp* varies step-wise from a low initial value to a higher one and then back to the initial one. The *Kp* profile for this simulation is shown in Figure 6. We chose *Kp* to be initially equal to 1.3 to simulate calm conditions. This initial state is the steady state calculated in the previous section. Then, *Kp* becomes equal to 4 for one day and finally it returns to its initial low value. Next, we will focus on the evolution of the electron distributions from time *T1* (initial state) to time *T2* (state after 1 day of *Kp* = 4) shown in Figure 6.

415

416 **4.2.1. PSD as a function of L shell**

417 When *Kp* increases, both radial diffusion and electron-chorus interactions are enhanced.
418 To identify which process is responsible for the dynamics observed we perform three
419 simulations: one where both radial diffusion and chorus interactions are included, one
420 where we 'turn off' radial diffusion and one where we 'turn off' electron-chorus
421 interactions. The initial state used is the same for all simulations. The results from the
422 three simulations at time *T2* are plotted in Figure 7. In this figure, phase space densities
423 are plotted versus L^* shell for equatorial particles with magnetic moment equal to 2100
424 MeV/G. Also marked (vertical dashed lines) is the plasmapause position for *Kp* = 1.3 and
425 *Kp* = 4.

426 When we 'turn off' radial diffusion, interactions with chorus waves are the only process
427 acting on radiation belt electrons outside the plasmasphere. As a result, at time *T2* phase
428 space densities increase significantly creating a very pronounced peak at $L^* = 5.7$. This
429 increase is confined in the region where chorus waves are defined in our simulation (*Lpp*
430 $< L^* < 6.5$) and is maximal in the $L^* = 5\text{-}6$ region (increase of more than 2 orders of
431 magnitude).

432 When we 'turn off' electron-chorus interactions, radial diffusion is the only process
433 acting on electrons outside the plasmasphere. In this case, at time *T2* phase space
434 densities decrease at higher L^* shells ($L^* > 4.5$) and increase at lower L^* shells. This is the
435 result of particles diffusing away from the peak that already exists in the initial state.
436 During high activity conditions, enhanced outward radial diffusion from the peak- at $L^* \sim$
437 5- towards higher L^* results in the decrease of PSD since particles are lost at the boundary

438 (which stays constant in our simulation). Inward radial diffusion is weaker, but we can
439 see a small increase in PSD at $L^* < 4.5$.
440 Finally, when both processes are included in the simulation, the localized effect of
441 chorus waves is diffused by radial diffusion to all L^* shells. The peak value decreases
442 while values around the peak increase. This increase is more important at higher L^* shells
443 where radial diffusion is stronger, resulting at an important increase of PSD in the region
444 where chorus waves are not considered in the simulation ($L^* > 6.5$) [*Varotsou et al.,*
445 2005]. However, the most important increase in the PSD-L^* distribution- more than an
446 order of magnitude- is observed near $L^* = 5\text{-}6$ ($E = 1\text{-}2$ MeV).
447
448 **4.2.2. PSD as a function of equatorial pitch angle and energy**
449 In Figure 8, results from all three simulations ('turning off' chorus, 'turning off' radial
450 diffusion and including both processes) are plotted versus equatorial pitch angle at $L^* =$
451 5.2 and for $E = 1.7$ MeV particles. At this L^* we position ourselves at the peak of the
452 PSD distribution as shown in Figure 7 (red line).
453 Results agree well with those presented in Figure 7. Radial diffusion, when acting
454 alone, diffuses particles away from the peak in the initial PSD-L^* distribution decreasing
455 PSD at the peak location. This process is equally strong at all equatorial pitch angles-
456 since the D_{LL} coefficients do not depend on α_{eq}- but its effect depends also on $\partial f/\partial L$ at
457 each α_{eq} value.
458 When chorus interactions is the only process acting, PSD increases by a factor of ~ 100
459 for $\alpha_{eq} > 40$ degrees. Energy and pitch angle diffusion are much weaker at low equatorial
460 pitch angles for MeV electrons (see Figure 1 and 4).

When both processes are taken into account, radial diffusion weakens the effect of chorus waves for $\alpha_{eq} > 30$ degrees by diffusing particles away from the peak created by chorus interactions. However it is obvious that chorus interactions dominate over radial diffusion at $\alpha_{eq} > 30$ degrees and the overall result is a net increase of electron PSD (more than an order of magnitude) for these pitch angle values outside the plasmasphere.

In Figure 9, PSD is plotted versus energy (from 0.5 to 5 MeV) and equatorial pitch angle for $L^* = 5.2$ at times *T1* and *T2*. Phase space densities have greatly increased at time *T2* at the MeV energy range for $\alpha_{eq} > 30$ degrees in agreement with the results presented in Figure 8. However at lower pitch angle values no increase is observed for the MeV particles. To understand this behavior better we plot in Figure 10 for $Kp = 4$, as a function of energy, (a) pitch angle diffusion coefficients D_{yy} for $\alpha_{eq} = 85$ degrees (solid line) and $\alpha_{eq} = 30$ degrees (dash dot line) and (b) energy diffusion coefficients D_{EE} for $\alpha_{eq} = 90$ degrees (solid line) and $\alpha_{eq} = 30$ degrees (dash dot line).

For $\alpha_{eq} = 70$-90 degrees we do not expect pitch angle diffusion to play an important role, since, as it is noted in Section 4.1, the initial pitch angle distribution at *T1* is flat near these values. In this region, energy diffusion is principally responsible for the dynamics observed especially at higher energies as can be seen in Figure 10(b) for $\alpha_{eq} = 90$ degrees.

At $\alpha_{eq} = 30$ degrees the coefficient's values are very different from those at 90 degrees. Figure 10(b) shows that energy diffusion coefficients for high energy electrons become 10^3 times weaker (even more in some cases). As a result, the increase of high energy phase space densities in Figure 9 is much weaker at $\alpha_{eq} \sim 30$ degrees than at higher ones.

4.2.3. Fluxes

Since PSD is not a physical quantity that is measured by satellites, we show here our results for the dynamic test-case simulation including both radial diffusion and electron-chorus interactions as fluxes. In Figure 11, omnidirectional fluxes at the equator are shown in an L^*-time space for 1.6 MeV. The plasmapause location is shown with a green line and the *Kp* variation with time is shown on the top of the figure.

Once again we clearly observe the electron acceleration due to chorus interactions: MeV fluxes increase in the heart of the radiation belts when activity increases. After 1 day of $Kp = 4$ fluxes become 24 times higher at $L^* = 5.7$ and 15 times higher at $L = 6.6$. When *Kp* recovers to its initial low value, MeV fluxes keep increasing at $L^* > 6$ due to radial diffusion. After the plasmapause relaxes to its initial position MeV fluxes inside the plasmasphere decrease slowly.

5. Parametric study

In Sections 3 and 4 we presented the results of simulations including chorus interactions in the Salammbô 3D code. The results showed clearly that a low energy seed population can be locally accelerated by chorus waves to MeV energies in the heart of the radiation belts near $L^* = 5$. However, many of the parameters used in the simulations are quite uncertain, thus it is important to perform a parametric study where the sensitivity of the results to the parameter's values can be quantified. Here we examine how results change if we consider different values for three of the important parameters: 1) radial diffusion coefficients, 2) initial state condition and 3) source condition at $L^* = 8$.

5.1. Radial diffusion coefficients

507 The accurate definition of radial diffusion coefficients constitutes one of the most
508 important projects in radiation belt physics. Although many efforts have been made to
509 calculate them empirically [*Lanzerotti et al.*, 1970; *Lanzerotti and Morgan*, 1973;
510 *Holzworth and Mozer*, 1979; *Brautigam and Albert*, 2000; *Li*, 2004] and theoretically
511 [*Falthammar*, 1965, 1966; *Schulz and Lanzerotti*, 1974; *Brizard and Chan,* 2001; *Perry*
512 *et al.*, 2005], there is still a lot of uncertainty concerning their dependence in L, energy,
513 pitch angle and magnetic activity.

514 As noted in previous sections, the result of the simulation performed using both radial
515 diffusion and chorus interactions depends on the relative intensity of the two processes. If
516 radial diffusion coefficients had lower values than the ones used here [*Brautigam and*
517 *Albert*, 2000] then the effect of chorus waves on the electron distribution would be even
518 more important. Here we examine how results change if we consider higher radial
519 diffusion coefficient values.

520 To investigate the influence of the radial diffusion coefficient's uncertainty on our
521 results we perform two simulations, increasing D_{LL} by a factor of three and six,
522 respectively. The results of both simulations for the steady case are plotted in Figure
523 12(a), together with the previous result- with the nominal *Brautigam and Albert* [2000]
524 coefficient values. The steady case simulation is for Kp = 1.3 and for M = 2100 MeV/G
525 equatorial particles. The number of iterations used is the same for all simulations.

526 Figure 12(a) shows that there is an important difference between the results of the three
527 simulations. When higher values are used for the radial diffusion coefficients, PSD
528 profiles become much more flat, or completely flat for the case where D_{LL} is increased by

a factor of 6. Radial diffusion erases almost completely the effect of chorus wave interactions by diffusing particles away from the peak that tends to be created.

In Figure 12(b), results from the dynamic simulations are plotted versus L^* for 2100 MeV/G equatorial electrons. The dynamic simulation performed here is the same dynamic test-case simulation as the one presented in Section 4.2: starting from an initial low activity state (steady state for Kp = 1.3) we calculate the state of the electron radiation belts after 1 day of high magnetic activity (1 day of Kp = 4). For the simulations presented here, the common initial state used is a flat PSD distribution which corresponds to the steady state calculated by using six times higher D_{LL} values.

Results after one day of Kp = 4 (time *T2*) are presented for the three different D_{LL} values. The first thing that we notice is that even when an initial flat distribution is used, irrespective of the size of D_{LL} used, the effect of chorus waves is easily distinguishable: electrons are locally accelerated to MeV energies and a peak forms near L^* = 5.

The differences between the three curves at time *T2* are at the location of the peak and at the level of PSD. When higher D_{LL} values are used, the peak is less pronounced, moves inwards in L^* and is characterized by lower PSD values. In these cases radial diffusion is more effective in diffusing particles away from the peak that chorus interactions tend to create. In addition, strong outward radial diffusion is more effective at high L^* values, thus the peak of the electron distribution is now observed at lower L^* shells.

5.2. Initial state condition

We compare the dynamics resulting after 1 day of Kp = 4 for two different initial state conditions as shown in Figure 13. State 1 has a flat L^*-profile and State 2 has a 'peaked'

552 L^*-profile with higher PSD values. From the comparison between dynamic state 1 (Dyn
553 1) and dynamic state 2 (Dyn 2) we conclude that phase space densities increase much
554 faster in the case where the flat, lower initial state is used, reaching peak values similar to
555 the ones for the case where the higher peaked initial state is used. The two initial states
556 are different by a factor of ~115 at the peak location ($L^* = 5.2$), however the two dynamic
557 states are different by only a factor of ~ 6.

558 The reason for this difference is the fact that radial diffusion will initially be much
559 weaker in the simulation using State 1, since $\partial f/\partial L = 0$ for all L^* values greater than $L^* =$
560 5. In this case, radial diffusion will become stronger only when a peak has started
561 forming due to chorus waves. However, in the simulation where State 2 is used, radial
562 diffusion will be strong from the beginning since significant peak in the PSD L^*-profile
563 exists initially.

564

565 **5.3. Boundary condition**

566 The outer boundary condition is an important parameter in the simulation. We chose to
567 use a characteristic energy of 2 keV for the plasma sheet which is the average value
568 measured at geosynchronous orbit [*Joseph Borovsky*, private communication 2007].
569 However, at geosynchronous altitude- near $L^* = 6.6$- it is also measured that this
570 temperature increases when magnetic activity increases, taking values of up to 5 keV
571 [*Joseph Borovsky*, private communication 2007].

572 In this Section we investigate the sensitivity of the simulation results to the boundary
573 condition. For this we consider two additional boundary conditions: one expressed by a
574 similar kappa distribution with characteristic energy of 5 keV (similar to the one used in

575 *Varotsou et al.*, [2005]) and one obtained empirically from CRRES measurements (used
576 in radial diffusion studies [*Shprits and Thorne, 2004; Shprits et al.*, 2005; *Shprits et al.,*
577 2006b]). The latter is defined by an exponential fit of the average flux measured by
578 CRRES at $L^* = 7$ and it is given by the expression
579
580 $$J = 8222.6 * 10^3 \exp\left(-E/0.141\right) \qquad (4)$$
581
582 Where J is the differential flux (in $cm^{-2}sr^{-1}MeV^{-1}s^{-1}$) and E is the kinetic energy of the
583 particle (in MeV). Differential fluxes at $L^* = 7$ are converted into PSD and then PSD
584 values are relaxed adiabatically to $L^* = 8$ by assuming that the particle's magnetic
585 moment is conserved. This assumption is based on the fact that only radial diffusion
586 occurs in the $L^* = 7$-8 region in the Salammbô code.
587 Both conditions are assumed to be constant with time like the one that was used in
588 simulations presented before (kappa distribution with $E_0 = 2$ keV). By keeping the
589 boundary condition constant we are able to clearly identify the effect of chorus waves on
590 the electron dynamics. The effect of a time dependent boundary condition is currently
591 being studied and will be presented in a future paper (see Discussion section).
592 The spectra of the three source conditions at the outer boundary are shown in Figure 14.
593 If a higher characteristic energy kappa distribution is considered, PSD of higher energies
594 increases and thus the $\partial f/\partial E$ values become smaller. As a result, we expect energy
595 diffusion to be less important for this case. The second boundary condition from CRRES
596 defines lower PSD values at low energies ($E < 100$ keV) and higher PSD values for $E =$
597 100 keV – 1 MeV, compared to those defined by the kappa distribution with $E_0 = 2$ keV.

598 We must note here that we extrapolated the CRRES spectrum for $E < 153$ keV since the
599 MEA detector only measured fluxes for energies higher than 153 keV. This may not be
600 the most realistic approach but provides us with another test case to study the effect of the
601 boundary condition on the MeV electron dynamics. To avoid any confusion we will call
602 this condition the modified CRRES boundary condition.
603 We have performed the same dynamic simulation as described in Section 4.2 for both
604 new boundary conditions. Results are presented in Figures 15 (a), (b) and (c) for 2100
605 MeV/G equatorial electrons for all three boundaries at times *T1* and *T2* of the dynamic
606 test-case simulation. First thing we observe is that all boundary conditions produce a
607 local peak in the PSD L^*-profile at time *T2* at similar locations- near $L^* = 5$. The most
608 important difference can be noted for the case when the modified CRRES condition is
609 used. For this case, the increase of PSD is less important than in the other two cases, even
610 though a higher energy source is defined. This is due to the fact that the energy spectrum
611 defined by this condition determines lower and flatter phase space densities at energies
612 lower than 100 keV. As a result, the source is smaller and the energy diffusion due to
613 chorus wave interactions weaker.
614 However, a higher energy spectrum at the source does not affect the amount of
615 energization. Differences observed between Figure 15(a) and (b) at time *T2* are due to the
616 difference in the initial states at time *T1* (see section 5.2).
617

618 **6. Discussion**

619 The conclusions of our study are clearly shown and supported throughout this paper,
620 however, our simulations have important limitations. One of the first and most important

assumptions that we made was that chorus waves are confined near the equator. Adding the effect of chorus waves at higher latitudes will affect the acceleration rate of electrons but also their losses since losses are mostly determined by the value of $D_{\alpha\alpha}$ near the edge of the loss cone [*Shprits et al.,* 2006a]. Various observations have shown that chorus waves are present at higher latitudes [*Tsurutani and Smith*, 1977; *Meredith et al.*, 2003b]. *Meredith et al*. [2003b] used CRRES data to show that dayside chorus waves are mostly confined to higher latitudes (λ > 15 degrees) in contrast to night side chorus which are mostly confined near the equator. When *Li et al.* [2007] introduced dayside high latitude chorus (parallel propagating only), together with night side equatorial chorus, into their 2D simulations MeV losses at high latitudes became important, however the net result was still electron acceleration.

Another limitation of our simulation is imposed by the fact that energy and pitch angle diffusion coefficients due to chorus interactions are limited to a certain L^* space. Recent observations have shown that chorus wave emissions can be detected at L^* shells up to $L^* = 10$ [*Santolík et al.*, 2005], however in our simulations they are confined at $L^* < 6.5$. This prevents us from estimating the relative power of chorus interactions and radial diffusion outside $L^* = 6.2$, which is the last grid point inside $L^* = 6.5$ in Salammbô.

In addition, diffusion coefficients due to chorus interactions are defined for three *Kp* categories: $Kp < 2$, $2 \leq Kp < 4$ and $Kp \geq 4$. The first two categories are small but the third one is very broad (from 4 to 9) and it is the one that interests us the most. This broad categorization is due to limited statistics for $Kp \geq 4$. However, radial diffusion coefficients continuously increase with increasing geomagnetic activity. The *Kp*

643 categorization for the chorus wave effect makes it hard to directly compare with the
644 radial diffusion effect, especially if we want to simulate higher than $Kp = 4$ storms.
645 The precision of the Kp parameterization of wave intensity and f_{pe}/f_{ce} using the CRRES
646 data can also be questioned. In the first half of the mission, when the satellite was on the
647 dayside (at dawn), activity was weak, however, on the second half of the mission, when
648 the satellite was on the night side (at dusk), activity was high. For this second part, chorus
649 activity for low Kp values may be overestimated. In addition, as it can be seen in Figure 1
650 of *Meredith et al.* [2003b], there exists an important data gap above $L^* = 5$ near $MLT =$
651 10.
652 These limitations are also pointed out by *Maget et al.* [2007] when they run the
653 Salammbô 3D code using data assimilation techniques and found that when they included
654 chorus wave interactions in the scheme, fluxes were overestimated in the region inside L
655 = 4 as compared to the CRRES data.
656 More wave observations are needed for the better definition and understanding of the
657 region where chorus waves are interacting with electrons, their relation to magnetic
658 activity and their propagation characteristics. Many current observational studies focus
659 on the determination of the source and spatial distribution of chorus emissions using data
660 from POLAR [*Kristine Sigsbee*, private communication 2007], CLUSTER and DOUBLE
661 STAR [*Santolík et al.*, 2004, 2005]. More data will be available in the future with the
662 upcoming Radiation Belt Storm Probes mission.
663 We also think that the dependence of radial diffusion coefficients on energy and pitch
664 angle need to be further investigated. In the work presented here we chose to use the
665 diffusion coefficients estimated by *Brautigam and Albert* [2000] since these are the

666 values generally used by the radiation belt community. These coefficients depend on *L*-
667 shell and magnetic activity (*Kp* parameter). *Varotsou et al.* [2005] used radial diffusion
668 coefficients based on calculations by *Schulz* [1991] that are energy, pitch angle and L
669 dependent. A magnetic activity dependence was added based on a calculation using data
670 from the CRRES satellite. Magnetic radial diffusion coefficients by *Schulz* [1991]
671 become ~ 7 times weaker at α_{eq} = 20 degrees compared to their equatorial values. Thus,
672 results presented in this paper are similar to the ones presented by *Varotsou et al.* [2005]
673 for equatorial mirroring particles but different results are obtained for low α_{eq} values (not
674 shown in *Varotsou et al*. [2005]). In the case where coefficients by *Schulz* [1991] are
675 used, we don't observe the decrease at α_{eq} < 30 degrees, as seen in Figure 8, in Section
676 4.2.2. Recently, *Perry et al*. [2005] calculated radial diffusion coefficients by
677 incorporating spectral characteristics of Pc5 waves into 3D simulations using the guiding
678 center approximation. They found that when a data-based, frequency and *L*-dependent
679 model is used for the wave power, an important decrease in radial diffusion coefficients
680 occurs as the mirror latitude increases from 0 degrees (equator) to 20 degrees.

681 Finally, we must note the absence of the cross diffusion coefficient $D_{\alpha E}$ in equation (2).
682 The effect of this coefficient on the final result is still a subject of discussion. The high
683 values of the coefficient as calculated by the PADIE code [*Glauert and Horne*, 2005]-
684 sometimes even higher than the energy diffusion coefficient- suggest that its effect will
685 be important. A recent study by *Albert and Young* [2005] showed that when the cross
686 term is introduced in the diffusion equation results are qualitatively similar, but for small
687 α_{eq} energy diffusion is overestimated if the cross diffusion is neglected. The cross
688 diffusion term is not included in any current 3D radiation belt code.

689 Our current priority is to validate the new code by simulating a real storm. A more
690 realistic study of the radiation belt dynamics during geomagnetic storm conditions, where
691 the *Kp* and boundary variation are taken from real data, is currently being performed and
692 will be presented in a future paper.
693 Another important development of our code is the introduction of higher latitude day
694 side chorus. As discussed above, these waves are expected to introduce MeV electron
695 losses into the loss cone.
696 In addition, other wave types are currently being studied for introduction in the
697 Salammbô code. Recent studies have shown that enhanced EMIC waves in plasmaspheric
698 plumes formed during the storm's main phase (e.g., *Erlandson and Ukhorskiy*, 2001) can
699 cause strong MeV electron losses from pitch angle diffusion in the loss cone (*Thorne and*
700 *Kennel*, 1971; *Albert*, 2003; *Summers and Thorne*, 2003). Plasmaspheric hiss is currently
701 included in the code but it is independent of geomagnetic activity. Our current goal is to
702 introduce activity dependent hiss, since studies have shown that hiss is enhanced during
703 active conditions [*Meredith et al.,* 2004].
704 Finally, we want to underline the importance of comparing results obtained from
705 different codes. We hope that in the future we will be able to work with other teams in
706 comparing simulation results. However this has to be done with much caution since the
707 assumptions considered in each model are different.
708
709 **7. Conclusions**
710 We have run steady state and dynamic test-case simulations to study the effect of
711 electron-chorus resonant interactions on the radiation belt electron dynamics. We used

712 the Salammbô 3D physical model which includes radial diffusion and particle-wave
713 interactions inside and outside of the plasmasphere. Simulations were performed where
714 both electron-chorus interactions and radial diffusion were included in the code but we
715 also run simulations with only one of the two processes included. In that way we were
716 able to identify the role of each of these two key physical processes on the radiation belt
717 dynamics. The main results of our study are the following:

718 1. The introduction of chorus interactions in the Salammbô code leads to the local
719 acceleration of electrons to MeV energies.
720 2. Acceleration during dynamic test-case simulations of moderate activity conditions
721 (Kp = 4) is stronger at L^* ~5 and for equatorial pitch angles near 90 degrees.
722 3. The net effect of a geomagnetic storm- the peak value and location- is defined by
723 the relative power between chorus interactions and radial diffusion.
724 4. Simulation results are not sensitive to the high energy distribution of the source,
725 however they are sensitive to the low energy distribution (E < 100 keV).

726 Our results support the following scenario: during active geomagnetic periods low
727 energy electrons are transported inwards from an outer source location by enhanced
728 convection and radial diffusion, a fraction of them are energized locally to MeV energies
729 by chorus interactions. At the same time radial diffusion acts diffusing particles inwards
730 and outwards from the peak that tends to form in the PSD distribution.

731 **References**

732 Abel, B. and R. M. Thorne (1998a), Electron scattering loss in Earth's inner
733 magnetosphere 1. Dominant physical processes, *J. Geophys. Res., 103,* 2385.

734 Abel, B. and R. M. Thorne (1998b), Electron scattering loss in Earth's inner
735 magnetosphere 2. Sensitivity to model parameters, *J. Geophys. Res., 103,* 2397.

736 Albert, J. M., and S. L. Young (2005), Multidimensional quasi-linear diffusion of
737 radiation belt electrons, *Geophys. Res. Lett.*, *32*, L14110, doi:10.1029/2005GL023191.

738 Anderson, R. R., D. A. Gurnett, and D. L. Odem (1992), CRRES plasma wave
739 experiment, *J. Spacecr. Rockets*, *29*,(4), 570-573.

740 Beutier, T., and D. Boscher (1995), A three-dimensional analysis of the electron radiation
741 belt by the Salammbô code, *J. Geophys. Res., 100*, 14,853.

742 Beutier, T., D. Boscher, and Martin France (1995), SALAMMBO: A three-dimensional
743 simulation of the proton radiation belt, *J. Geophys. Res., 100*, 17,181.

744 Bourdarie, S., D. Boscher, T. Beutier, J.-A. Sauvaud, and M. Blanc (1996), Magnetic
745 storm modeling in the Earth's electron belt by the Salammbô code, *J. Geophys. Res.,*
746 *101*, 27,171-27,176.

747 Brautigam, D. H., and J. M. Albert (2000), Radial diffusion analysis of outer radiation
748 belt electrons during the October 9, 1990, magnetic storm, *J. Geophys. Res.*, *105*, 291.

749 Brizard, A. J., and Chan, A. A. (2001), Relativistic bounce-averaged quasi-linear
750 diffusion equation for low frequency electromagnetic fluctuations, *Phys. Of Plasmas*,
751 Vol. 8, 11, doi:10.1063/1.1408623.

752 Carpenter, D. L., and C. G. Park (1973), On what ionosphere workers should know about
753 the plasmapause-plasmasphere, *Rev. Geophys., 11*, 133.

754 Chen, Y., R. H. W. Friedel, and G. D. Reeves (2006), Phase space density distributions of
755 energetic electrons in the outer radiation belt during two Geospase Environment
756 Modeling Inner Magnetosphere/Storms selected storms, J. *Geophys. Res., 111*,
757 A11S04, doi:10.1029/2006JA011703.
758 Chen, Y., G. D. Reeves and R. H. W. Friedel (2007), The energization of relativistic
759 electrons in the outer Van Allen radiation belt, *Nature Physics*, doi:10.1038/nphys655.
760 Christon, S. P., D. G. Mitchell, D. J. Williams, L. A. Frank, C. Y. Huang, and T. E.
761 Eastman (1988), Energy spectra of plasma sheet ions and electrons from ~50eV/e to ~1
762 MeV during plasma temperature transitions, *J. Geophys. Res., 93*, 2562.
763 Christon, S. P., D. J. Williams, D. G. Mitchell, C. Y. Huang, and L. A. Frank (1991),
764 Spectral characteristics of plasma sheet ion and electron populations during disturbed
765 geomagnetic conditions, *J. Geophys. Res., 96*, 1.
766 Courant, R., K. Friedrichs, and H. Lewy (1967), On the Partial Difference Equations of
767 Mathematical Physics, *IBM J.* 11, 215-234.
768 Elkington, S. R., M. K. Hudson, and A. A. Chan (1999), Acceleration of relativistic
769 electrons vis drift-resonant interaction with toroidal-mode Pc-5 ULF oscillations,
770 *Geophys. Res. Lett.*, *26*, 3273-3276.
771 Fälthammar, C.G. (1965), Effects of time-dependent electric fields on geomagnetically
772 trapped radiation, *J. Geophys. Res., 70*, 2503.
773 Fälthammar, C.G. (1966), On the transport of trapped particles in the outer
774 magnetosphere, *J. Geophys. Res., 71*, 1487.

775 Fox, N. J., B. H. Mauk, and J. B. Blake (2006), Role of non-adiabatic processes in the
776 creation of the outer radiation belts, *Geophys. Res. Lett., 33*, L18108,
777 doi:10.1029/2006GL026598.
778 Friedel, R. H., G. D. Reeves, and T. Obara (2002), Relativistic electron dynamics in the
779 inner magnetosphere- A review, *J. Atmos. Sol. Terr. Phys.*, *64*, 265.
780 Glauert, S. A. and R. B. Horne (2005), Calculation of pitch angle and energy diffusion
781 coefficients with the PADIE code, *J. Geophys. Res., 110*, doi:10.1029/2004JA010851.
782 Green, J. C., and M. G. Kivelson (2004), Relativistic electrons in the outer radiation belt:
783 Differentiating between acceleration mechanisms, *J. Geophys. Res., 109*, A03213,
784 doi:10.1029/2003JA010153.
785 Hedin, A. E. (1979), Tables of thermospheric temperature, density and composition
786 derived from satellite and ground based measurements, *Rep. N79-18515, vol.1-3*,
787 NASA Goddard Space Flight Center, Greenbelt, Md.
788 Holzworth, R. H., and F. S. Mozer (1979), Direct evaluation of the radial diffusion
789 coefficient near L = 6 due to electric field fluctuations, *J. Geophys. Res.*, *84*, 2559.
790 Horne, R. B. (2002), The contribution of wave particle interactions to electron loss and
791 acceleration in the Earth's radiation belts during geomagnetic storms, in *USRI Review*
792 *of Radio Science 1999-2002*, edited by W. R. Stone, pp. 801-828, chap. 33, John Wiley,
793 Hoboken, N. J.
794 Horne, R. B., and R. M. Thorne (1998), Potential waves for relativistic electron scattering
795 and stochastic acceleration during magnetic storms, *Geophys. Res. Lett.*, *25,* 3011.

796 Horne, R. B., S. A. Glauert, and R. M. Thorne (2003a), Resonant diffusion of radiation
797 belt electrons by whistler-mode chorus, *Geophys. Res. Lett., 30*, 1493,
798 doi:10.1029/2003GL016963.
799 Horne, R. B., N. P. Meredith, R. M. Thorne, D. Heynderickx, R. H. A. Iles, and R. R.
800 Anderson (2003b), Evolution of energetic electron pitch angle distributions during
801 storm time electron acceleration to megaelectronvolt energies, *J. Geophys. Res., 108*,
802 1016, doi:10.1029/2001JA009165.
803 Horne, R. B., R. M. Thorne, Y. Y. Shprits, N. P. Meredith, S. A. Glauert, A. J. Smith, S.
804 G. Kanekal, D. N. Baker, M. J. Engebretson, J. L. Posch, M. Spasojevic, U. S. Inan, J.
805 S. Pickett, and P. M. E. Decreau (2005), Wave acceleration of electrons in the Van
806 Allen radiation belts, *Nature*, Vol 437, doi:10.1038/nature03939.
807 Jordanova, V. K., L. M. Kistler, J. U. Kozyra, G. V. Kazanov, and A. F. Nagy (1996),
808 Collisional losses of ring current ions, *J. Geophys. Res.*, *101*, 111.
809 Jordanova, V. K., A. Boonsiriseth, R. M. Thorne, and Y. Dotan (2003), Ring current
810 asymmetry from global simulations using a high-resolution electric field model, *J.*
811 *Geophys. Res.*, *108*(A12), 1443, doi:10.1029/2003JA009993.
812 Jordanova, V. K., and Y. S. Miyoshi (2005), Relativistic model of ring current and
813 radiation belt ions and electrons: Initial results, *Geophys. Res. Lett.*, *32*, L14104,
814 doi:10.1029/2005GL023020.
815 Iles, R. H. A., N. P. Meredith, A. N. Fazakerley, and R. B. Horne (2006), Phase space
816 density analysis of the outer radiation belt energetic electron dynamics, *J. Geophys.*
817 *Res.*, *111*, A03204, doi:10.1029/2005JA011206.
818 Kennel, C. F. (1969), Consequences of a magnetospheric plasma, *Rev. Geophys., 7*, 379.

819 Kennel, C. F., and F. Engelmann (1966), Velocity space diffusion from weak plasma
820 turbulence in a magnetic field, *Phys. Fluids, 9*, 2377.
821 Lanzerotti,L. J., and C. G. Morgan (1973), ULF geomagnetic power near L = 4-2:
822 Temporal variation of the radial diffusion coefficient for relativistic electrons, *J.*
823 *Geophys. Res.*, *78*,4600.
824 Lanzerotti, L. J., C. G. MacLennan, and M. Schulz (1970), Radial diffusion of outer-zone
825 electrons: An empirical approach to third-invariant violation, *J. Geophys. Res.*, *75*,
826 5351.
827 Li, X. (2004), Variations of 0.7-6.0 MeV electrons at geosynchronous orbit as a function
828 of solar wind, *Sp. Weather*, Vol. 2, No. 3, S0300610.1029/2003SW000017.
829 Li, W., Y. Y. Shprits, and R. M. Thorne (2007), Dynamic evolution of energetic outer
830 zone electrons due to wave-particle interactions during storms, *J. Geophys. Res.*,
831 accepted.
832 Lyons, L. R. (1974), General relations for resonant particle diffusion in pitch angle and
833 energy, *J. Plasma Phys., 12*, 45-49.
834 Maget, V., S. Bourdarie, D. Boscher, and R. H. W. Friedel (2007), Data assimilation of
835 LANL satellite data into the Salammbô electron code over a complete solar cycle by
836 direst insertion, *Sp. Weather*, 2007SW000322.
837 McIlwain, C.E. (1961), Coordinates for mapping the distribution of magnetically trapped
838 particles, *J. Geophys. Res., 66*, 3681-3691.
839 Meredith, N. P., R. B. Horne, and R. R. Anderson (2001), Substorm dependence of
840 chorus amplitudes: Implications for the acceleration of electrons tp relativistic energies,
841 *J. Geophys. Res.*, *106*, 13,165.

842 Meredith, N. P., R. B. Horne, R. H. A. Iles, R. M. Thorne, D. Heyndrickx, and R. R.
843 Anderson (2002a), Outer zone relativistic electron acceleration associated with
844 substorm-enhanced whistler-mode chorus, *J. Geophys. Res., 107*, 1144.
845 Meredith, N. P., R. B. Horne, D. Summers, R. M. Thorne, R. H. A. Iles, D. Heynderickx,
846 and R. R. Anderson (2002b), Evidence for acceleration of outer zone electrons to
847 relativistic energies by whistler mode chorus, *Ann. Geophys., 20*, 967.
848 Meredith, N. P., M. Cain, R. B. Horne, R. M. Thorne, D. Summers, and R. R. Anderson
849 (2003a), Evidence for chorus-driven electron acceleration to relativistic energies from a
850 survey of geomagnetically-disturbed periods, *J. Geophys. Res., 108*(A6), 1248,
851 doi:10.1029/2002JA009764.
852 Meredith, N. P., R. B. Horne, R. M. Thorne, and R. R. Anderson (2003b), Favored
853 regions for chorus-driven electron acceleration to relativistic energies in the Earth's
854 outer radiation belt, *Geophys. Res. Lett., 30*, 1871, doi:10.1029/2003GL017698.
855 Meredith, N. P., R. B. Horne, R. M. Thorne, D. Summers, and R. R. Anderson (2004),
856 Substorm dependence of plasmaspheric hiss, *J. Geophys. Res., 109,* A06209,
857 doi:10.1029/2004JA010387.
858 Miyoshi, Y., A. Morioka, T. Obara, H. Misawa, T. Nagai, and Y. Kasahara (2003),
859 Rebuilding process of the outer radiation belt during the 3 November 1993 magnetic
860 storm: NOAA and Exos-D observations, *J.Geophys. Res., 108*(A1), 1004,
861 doi:10.1029/2001JA007542.
862 Miyoshi, Y. S., V. K. Jordanova, A. Morioka, M. F. Thomsen, G. D. Reeves, D. S.
863 Evans, and J. C. Green (2006), Observations and modeling of energetic electron

dynamics during the October 2001 storm, *J. Geophys. Res.*, *111*, A11S02, doi:10.1029/2005JA011351.

Obara, T., T. Nagatsuma, M. Den, Y. Miyoshi, and A. Morioka (2000), Main-phase creation of 'seed' electrons in the outer radiation belt, *Earth Planets Space, 52*, 41-47.

O'Brien, T. P., R. L. McPherron, D. Sornette, G. D. Reeves, R. H. Friedel, and H. J. Singer (2001), Which magnetic storms produce relativistic electrons at geosynchronous orbit?, *J. Geophys. Res.*, *106*(8), 15,533, doi:10.1029/2001JA000052.

Perry, K. L., M. K. Hudson, and S. R. Elkington (2005), Incorporating spectral characteristics of Pc5 waves into three-dimensional radiation belt modeling and the diffusion of relativistic electrons, *J. Geophys. Res.*, *110*, A03215.

Reeves, G. D., D. N. Baker, R. D. Belian, J. B. Blake, T. E. Cayton, J. F. Fennell, R. H. W. Friedel, M. M. Meier, R. S. Selesnick and H. E. Spence (1998), The global response of relativistic radiation belt electrons to the January 1997 magnetic cloud, *Geophys. Res. Lett., 25*(17), 3265.

Reeves, G. D., K. L. McAdams, R. H. Friedel, and T. P. O'Brien (2003), Acceleration and loss of relativistic electrons during geomagnetic storms, *Geophys. Res. Lett.*, *30*(10), 1529, doi:10.1029/2002GL016513.

Roederer, J. G., Dynamics of Geomagnetically Trapped Radiation, Springer-Verlag, New York, 1970.

Santolík, O., D. A. Gurnett, and J. S. Pickett (2004), Multipoint investigation of the source region of storm-time chorus, *Ann. Geophys.*, 22, 2555-2563.

Santolík, O., E. Macúšová, K. H. Yearby, N. Cornilleau-Wenhrlin, and H. StC. K. Alleyne (2005), Radial variation of whistler-mode chorus: first results from the

887 STAFF/DWP instrument on board the Double Star TC-1 spacecraft, *Ann. Geophys.*, 23,
888 2937-2942.
889 Schulz, M. (1991), The magnetosphere, geomagnetically trapped radiation, in
890 *Geomagnetism*, vol. 4, edited by J. A. Jacobs, pp. 202-256, Elsevier, New York.
891 Schulz, M., and L. Lanzerotti (1974), Particle Diffusion in the Radiation Belts, Springer,
892 New York.
893 Shprits, Y. Y., and R. M. Thorne (2004), Time dependent radial diffusion modeling of
894 relativistic electrons with realistic loss rates, *Geophys. Res. Lett., 31*, L08805,
895 doi:10.1029/2004GL019591.
896 Shprits Y. Y., and R. M. Thorne (2006a), Controlling effect of the pitch angle scattering
897 rates near the edge of the loss cone on the electron lifetime, *J. Geophys. Res.*, *111*,
898 A12206, doi:10.1029/2006JA011758.
899 Shprits Y. Y., R. M. Thorne, R. Friedel, G. D. Reeves, J. Fennell, D. N. Baker, S. G.
900 Kanekal (2006b), Outward radial diffusion driven by losses at the magnetopause, *J.*
901 *Geophys. Res.*, *111*, A11214, doi:10.1029/2006JA011657.
902 Shprits Y. Y., R. M. Thorne, R. B. Horne, S. A. Glauert, M Cartwright, C. T. Russel, D.
903 N. Baker, S. G. Kanekal (2006c), Acceleration mechanism responsible for the
904 formation of the new radiation belt during the 2003 Halloween solar storm, *Geophys.*
905 *Res. Lett*., *33*, L05104, doi:10.1029/2005GL024256.
906 Shprits, Y. Y., R. M. Thorne, G. D. Reeves, and R. H. Friedel (2005), Radial diffusion
907 modeling with empirical lifetimes: comparison with CRRES observations, *Ann.*
908 *Geophys.*, 23, 1467-1471.

909 Summers, D., R. M. Thorne, and F. Xiao (1998), Relativistic theory of wave-particle
910 resonant diffusion with application to electron acceleration in the magnetosphere, *J.*
911 *Geophys. Res., 103*, 20,487.
912 Thorne, R. M., E. J. Smith, K. J. Fiske, and S. R. Church (1974), Intensity variation of
913 ELF hiss and chorus during isolated substorms, *Geophys. Res. Lett., 1*, 193-196.
914 Tsurutani, B. T. and E. J. Smith (1977), Two types of magnetospheric chorus and their
915 substorm dependencies, *J. Geophys. Res.*, *82*, 5112.
916 Vacaresse, A, D. Boscher, S. Bourdarie, M. Blanc, and J.-A. Sauvaud (1999), Modeling
917 the high-energy proton belt, *J. Geophys. Res., 104*, 28,601.
918 Van Allen, J.A., G.H. Ludwig, E.C. Ray, and C.E. McIlwain (1958), Observations of
919 high intensity radiations by satellites 1958 alpha and gamma, *Jet. Propul.*, *28*, 588.
920 Varotsou, A., D. Boscher, S. Bourdarie, R. B. Horne, S. A. Glauert, and N. P. Meredith
921 (2005), Simulation of the outer radiation belt electrons near geosynchronous orbit
922 including both radial diffusion and resonant interaction with Whistler-mode chorus
923 waves, *Geophys. Res. Lett., 32*, L19106, doi:10.1029/2005GL023282.

924 **Figure captions**

925 **Figure 1.** Energy and pitch angle diffusion coefficients due to chorus interactions, as a
926 function of energy and equatorial pitch angle for three *Kp* categories at $L^* = 4.8$.

927 **Figure 2.** Steady state phase space density calculation (in $MeV^{-3}s^{-3}$) for 2100 MeV/G
928 equatorial particles and *Kp* = 1.3, for two simulations: (a) including chorus wave
929 interactions and (b) including only radial diffusion.

930 **Figure 3.** Steady state phase space density (in $MeV^{-3}s^{-3}$) as a function of equatorial pitch
931 angle for 1.7 MeV electrons at $L^* = 5.2$ and for *Kp* = 1.3, for two simulations: (a)
932 including chorus wave interactions (red line) and (b) including only radial diffusion (blue
933 line).

934 **Figure 4.** Energy and pitch angle diffusion coefficients (in s^{-1}) as a function of equatorial
935 pitch angle, for $L^* = 5.2$, $E = 1.7$ MeV and $Kp = 1.3$.

936 **Figure 5.** Steady state phase space density (in $MeV^{-3}s^{-3}$) as a function of energy for
937 equatorial particles at $L^* = 5.2$ and for *Kp* = 1.3, for two simulations: including chorus
938 wave interactions (red line) and including only radial diffusion (blue line).

939 **Figure 6.** *Kp* profile for the dynamic test-case simulation.

940 **Figure 7.** Phase space densities (in $MeV^{-3}s^{-3}$) for 2100 MeV/G equatorial electrons as a
941 function of L^* from the three simulations at time *T2*: including only chorus wave
942 interactions (orange line), including only radial diffusion (blue line) and including both
943 processes (red line), starting from the same initial state (black line). Dashed lines show
944 the position of the plasmapause for *Kp* = 1.3 and *Kp* = 4.

945 **Figure 8.** Phase space densities (in $MeV^{-3}s^{-3}$) for 1.7 MeV electrons at $L^* = 5.2$ as a
946 function of equatorial pitch angle from the three simulations at time *T2*.

Figure 9. 2D plots of phase space densities at $L^* = 5.2$ as a function of energy (shown from 0.5 to 5 MeV on a log scale) and equatorial pitch angle at a) time T1 and b) time T2.

Figure 10. Diffusion coefficients as a function of energy for $Kp = 4$ and $L^* = 5.2$: (a) pitch angle diffusion coefficients at $\alpha_{eq} = 85$ degrees (solid line) and 30 degrees (dash dot line) and (b) energy diffusion coefficients at $\alpha_{eq} = 90$ degrees (solid line) and 30 degrees (dash dot line).

Figure 11. Omnidirectional equatorial flux variation during the test-case simulation for 1.6 MeV electrons. The plasmapause position is marked with a green line.

Figure 12. Phase space densities (in $MeV^{-3}s^{-3}$) for 2100 MeV/G equatorial particles as a function of L^* for (a) the three steady state simulations and (b) at time *T2* for the three dynamic simulations starting from the same initial state at *T1* (black line).

Figure 13. Phase space densities (in $MeV^{-3}s^{-3}$) for 2100 MeV/G equatorial particles as a function of L^* at times *T1* and *T2* from two dynamic simulations: one starting from State 1 and one starting from State 2.

Figure 14. Spectrum of the three distributions used as a source at the outer boundary ($L^* = 8$): the kappa distribution with $E_0 = 2$ keV (red line), the kappa distribution with $E_0 = 5$ keV (blue line) and the modified CRRES distribution (black line).

Figure 15. Phase space densities (in $MeV^{-3}s^{-3}$) for 2100 MeV/G equatorial particles as a function of L^* at times *T1* and *T2* using the three boundary conditions: (a) a kappa distribution with $E_0 = 2$ keV, (b) the kappa distribution with $E_0 = 5$ keV and (c) the modified CRRES distribution.

969 **Table1. Diffusive processes in Salammbô**

Physical Process (1)	Effect (2)	Coefficients (3)	Calculation (4)	Parameters (5)
Field fluctuations	Radial Diffusion	$D_{LL}^{(m)}$	*Brautigam and Albert* (2000)	*Brautigam and Albert* (2000)
Particle-wave interactions *inside* plasmasphere	Pitch angle diffusion	D_{yy}	*Abel and Thorne* (1998a)	Described in: *Abel and Thorne* (1998b)
Coulomb collisions with high atmosphere	Pitch angle diffusion	D_{yy}	*Schulz and Lanzerotti (1974)*	Atmospheric densities from MSIS 86 model[a] [*Hedin*, 1979]
Particle-wave interactions *outside* plasmasphere	Energy diffusion and pitch angle diffusion	D_{EE}, D_{yy}	PADIE code: *Glauert and Horne* (2005)	CRRES data: Glauert and Horne (2005) and Meredith et al. (2003b)

970 [a] Plus a hydrostatic model above 800 km for each species

971

972 **Table 1.** Physical processes included in Salammbô, their effect on radiation belt
973 electrons, the coefficients that express their effect in the diffusion equation and the
974 references for the calculation and the parameters used to estimate the coefficients.

975 **Table 2. Chorus wave characteristics**

Parameter	Assumed distribution	Characteristic values
Wave power	Gaussian distribution	Peak: $0.35f_{ce}$ Bandwidth: $0.15fce$ Lower cut-off: $0.125fce$ Upper cut-off: $0.575fce$
Wave normal angle	Gaussian distribution $X = \tan(\psi)$	Peak: $X_m = 0$ Angular spread: $X_w = \tan(30^0)$ $X_{min} = 0$ $X_{max} = 1$

976

977 **Table 2.** The wave characteristics used for the calculation of the pitch angle and energy

978 diffusion coefficients due to chorus wave interactions.

Table 3. Diffusive processes outside the plasmapause

Diffusive process	Coefficients	Domain of application
Radial Diffusion	$D_{LL}= 10^{(0.506Kp-9.325)} L^{10}$	applied everywhere in our simulation domain
Pitch-angle and energy diffusion due to chorus waves	PADIE coefficient matrix for $D_{\alpha\alpha}$ and D_{EE} for 3 *Kp* categories	Plasmapause < $L \leq 6.5$ 10 keV $\leq E \leq$ 3MeV all α_{eq} values

Table 3. The two diffusive physical processes included in Salammbô outside the plasmapause, their expressions and the simulation domain of application.

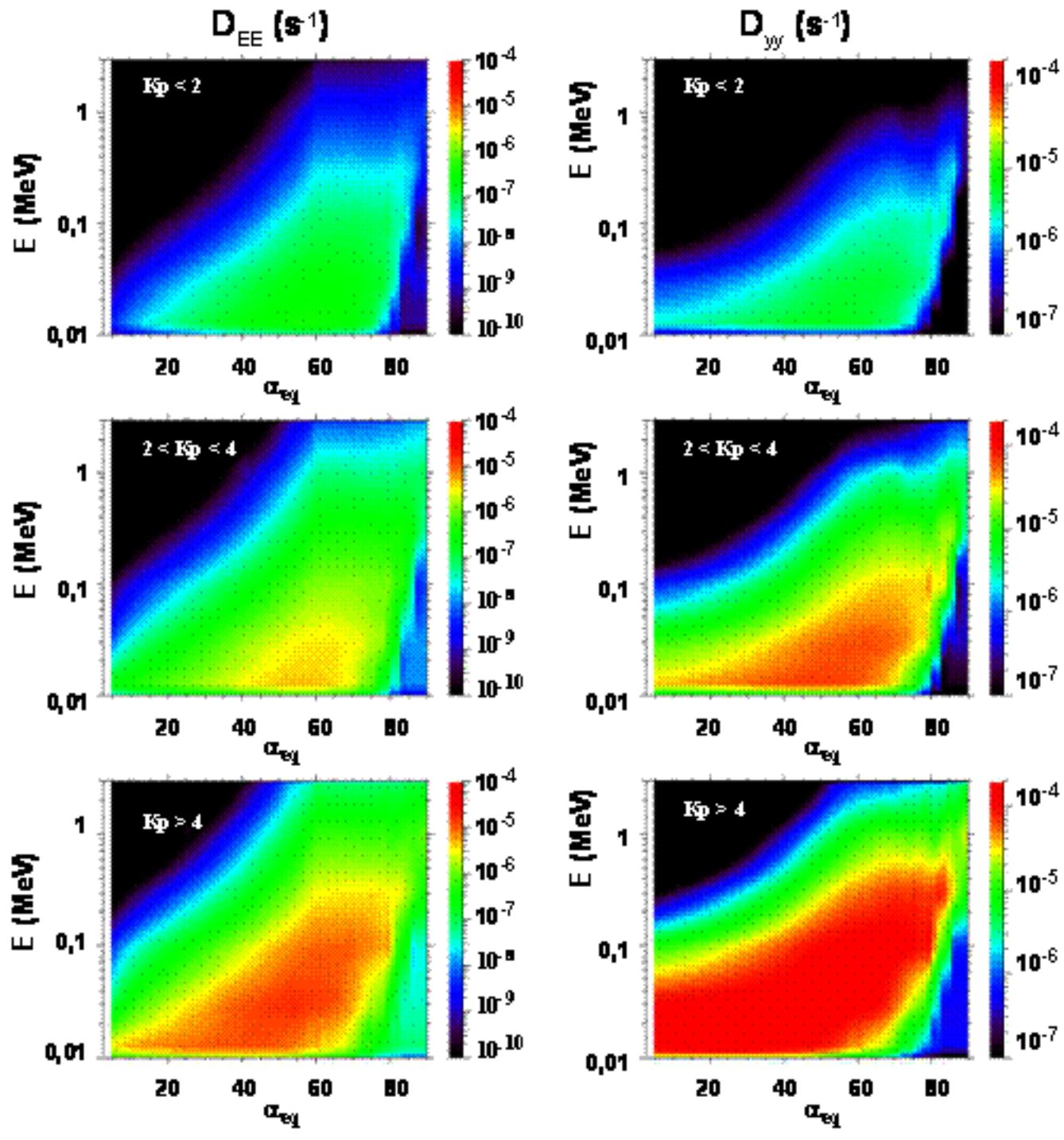
D_{EE} (s^{-1})
D_{yy} (s^{-1})
Kp < 2
2 < Kp < 4
Kp > 4
E (MeV)
1
0,1
0,01
20
40
60
80
α_{eq}
10^{-4}
10^{-5}
10^{-6}
10^{-7}
10^{-8}
10^{-9}
10^{-10}

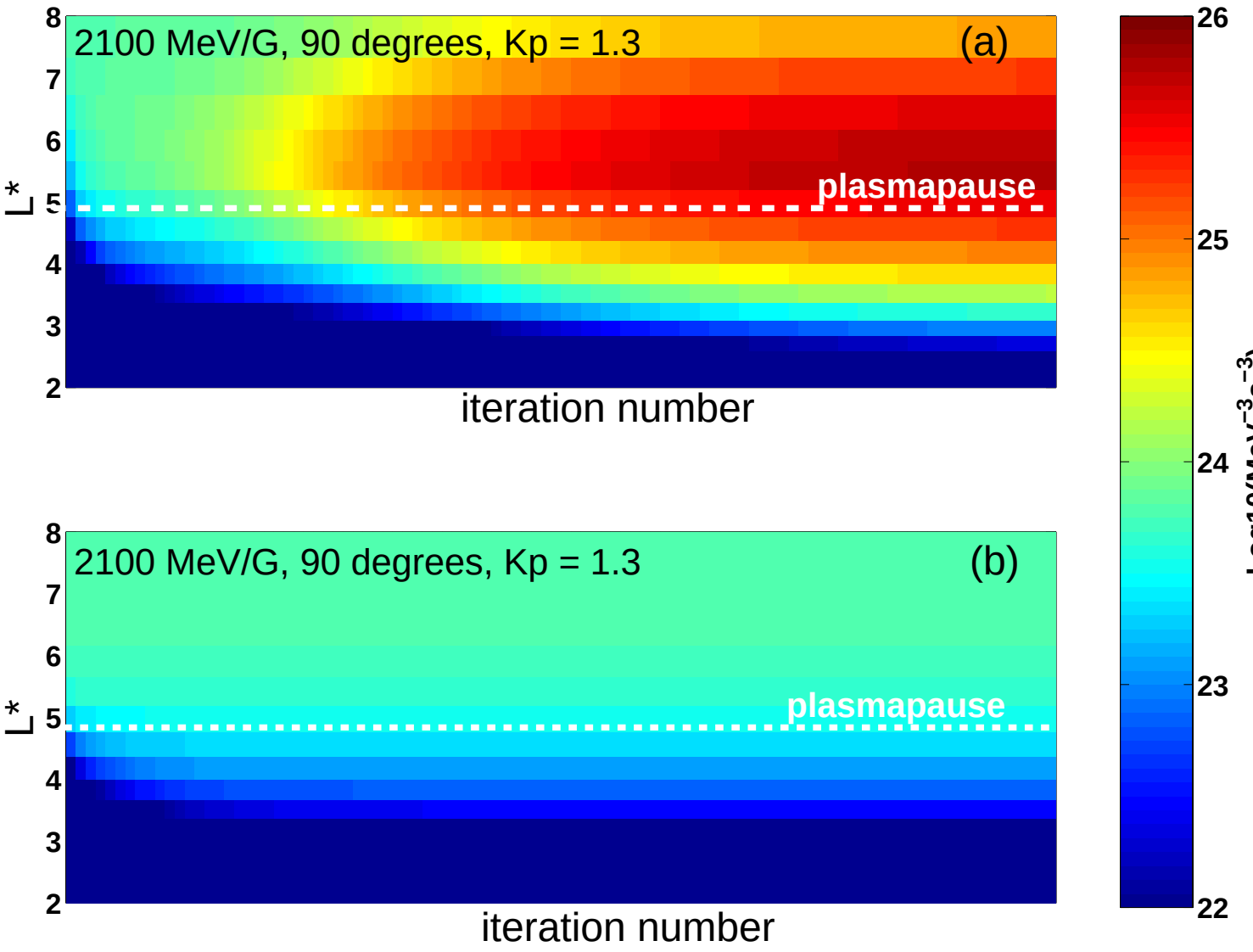

Figure 2. Steady state phase space density calculation (in MeV−3 s−3) for 2100 MeV/G equatorial particles and Kp = 1.3, for two simulations: (a) including chorus wave interactions and (b) including only radial diffusion.

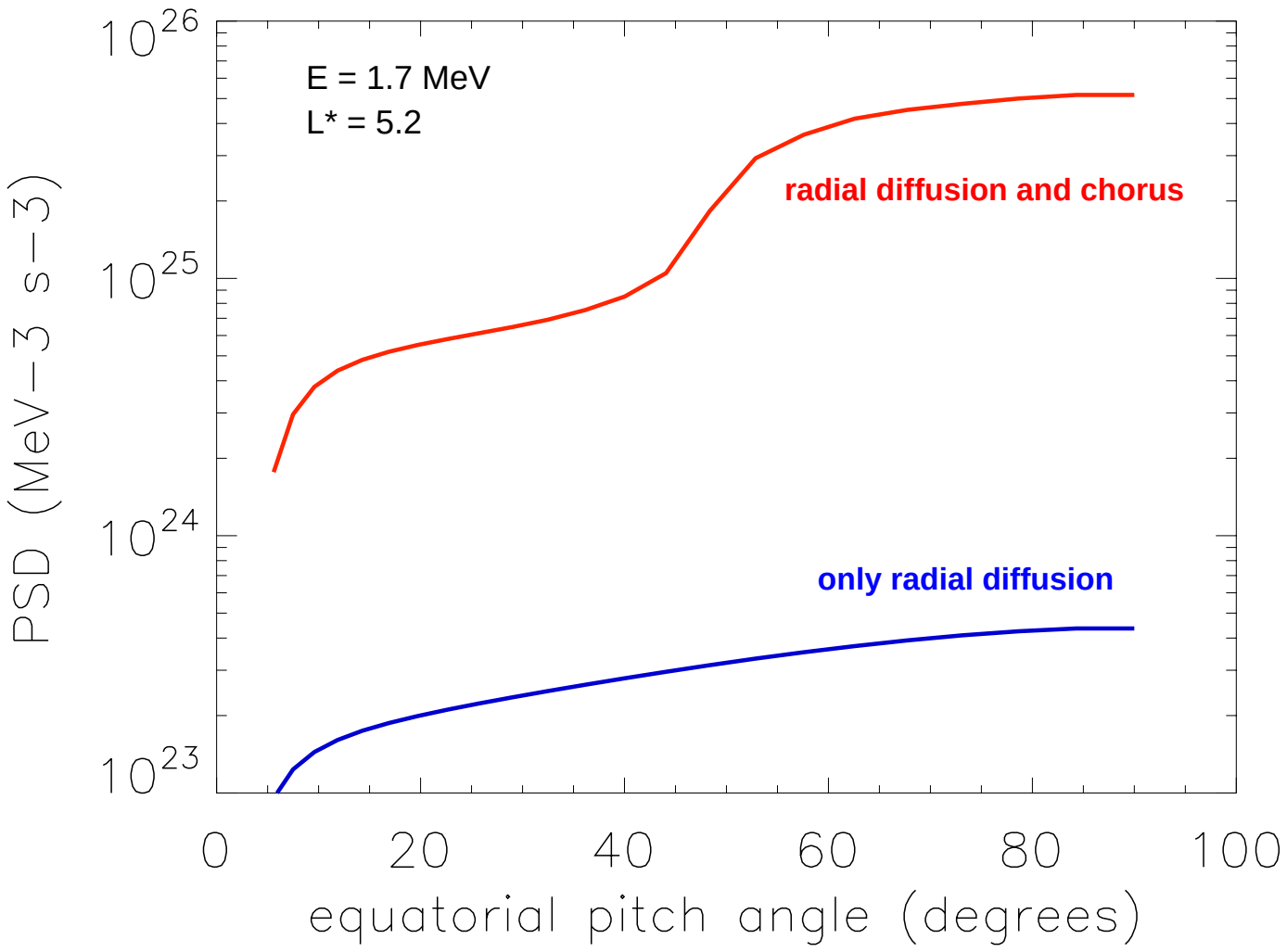

Figure 3. Steady state phase space density as a function of equatoral pitch angle for 1.7 MeV electrons at L* = 5.2 and for Kp = 1.3, for two simulations: (a) including chorus wave interactions (red line) and (b) including only radial diffusion (blue line).

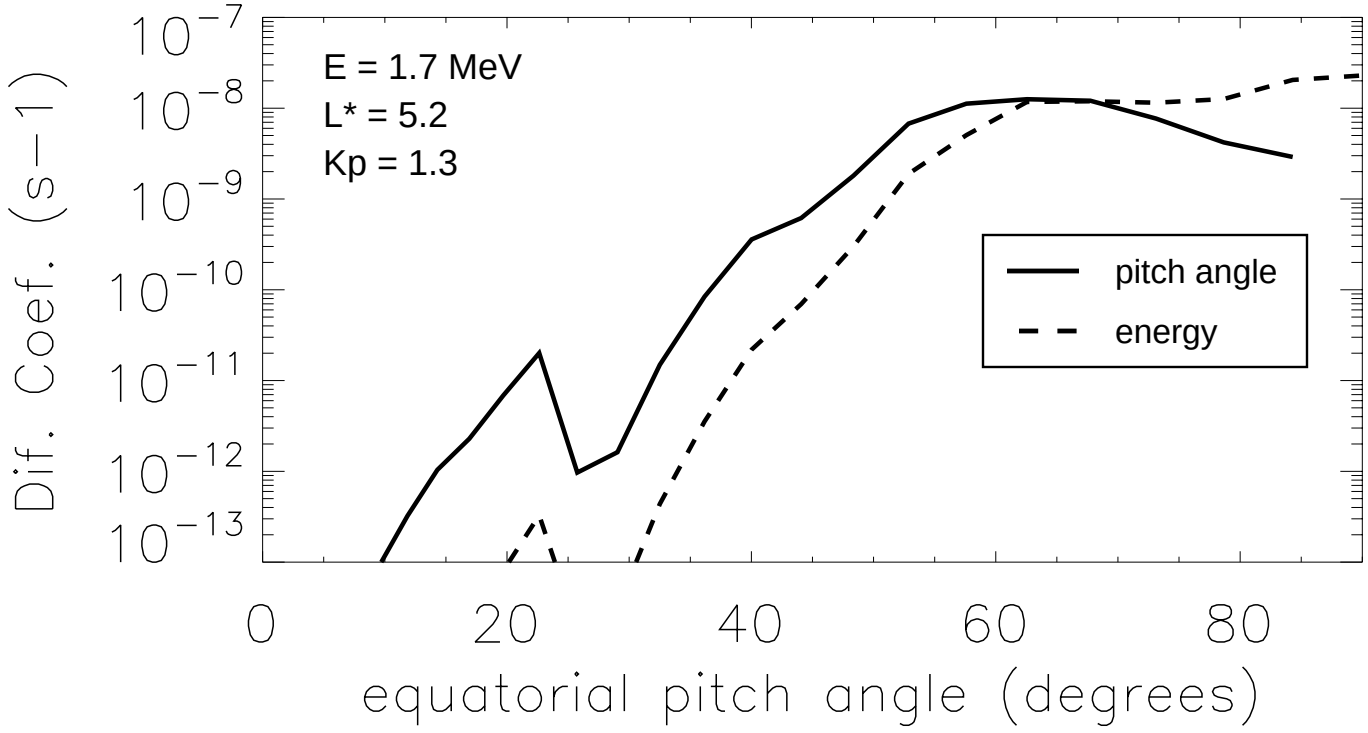

Figure 4. Energy and pitch angle diffusion coefficients (in s−1) as a function of equatorial pitch angle, for L* = 5.2, E = 1.7 MeV and Kp = 1.3.

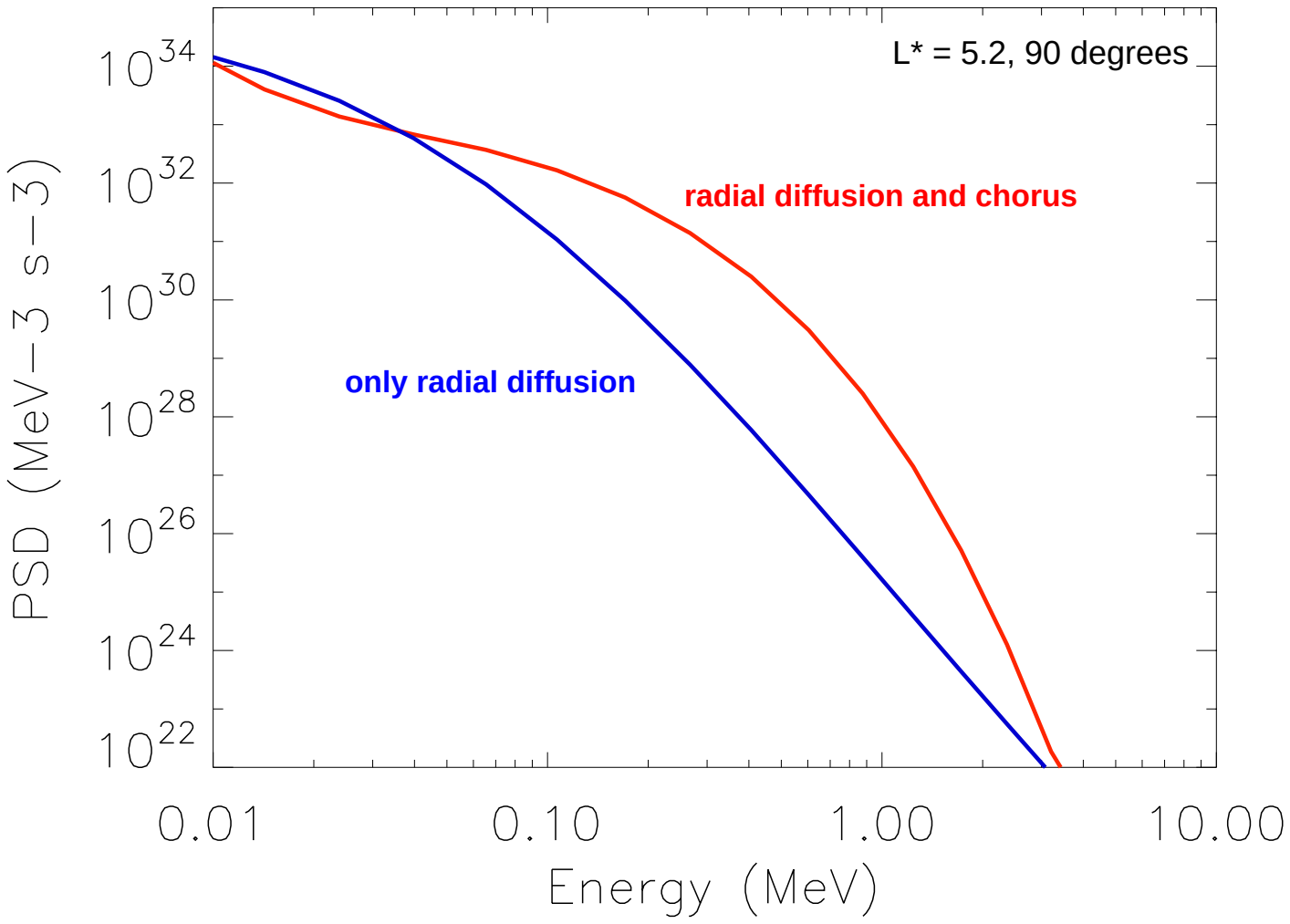

Figure 5. Steady state phase space density (in MeV−3 s−3) as a function of energy for equatorial particles at L* = 5.2 and for Kp = 1.3, for two simulations: including chorus wave interactions (red line) and including only radial diffusion (blue line).

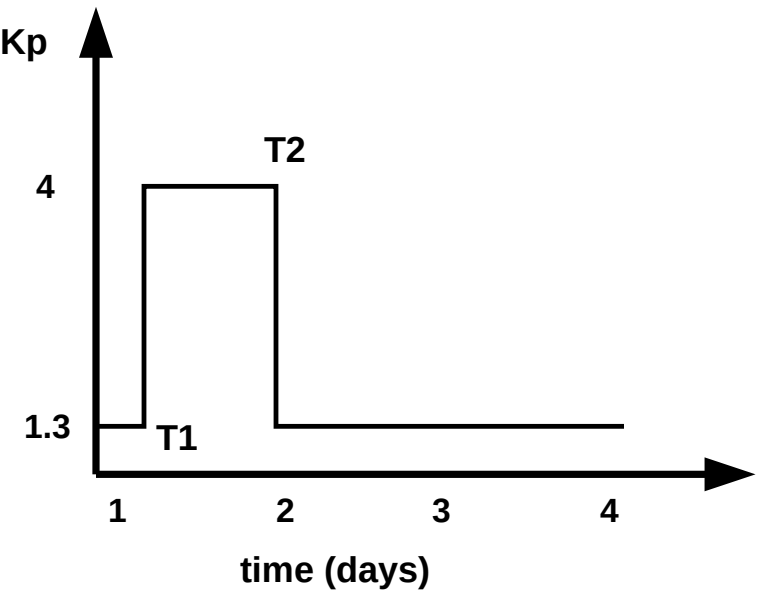

Figure 6. Kp profile for the dynamic test case simulation.

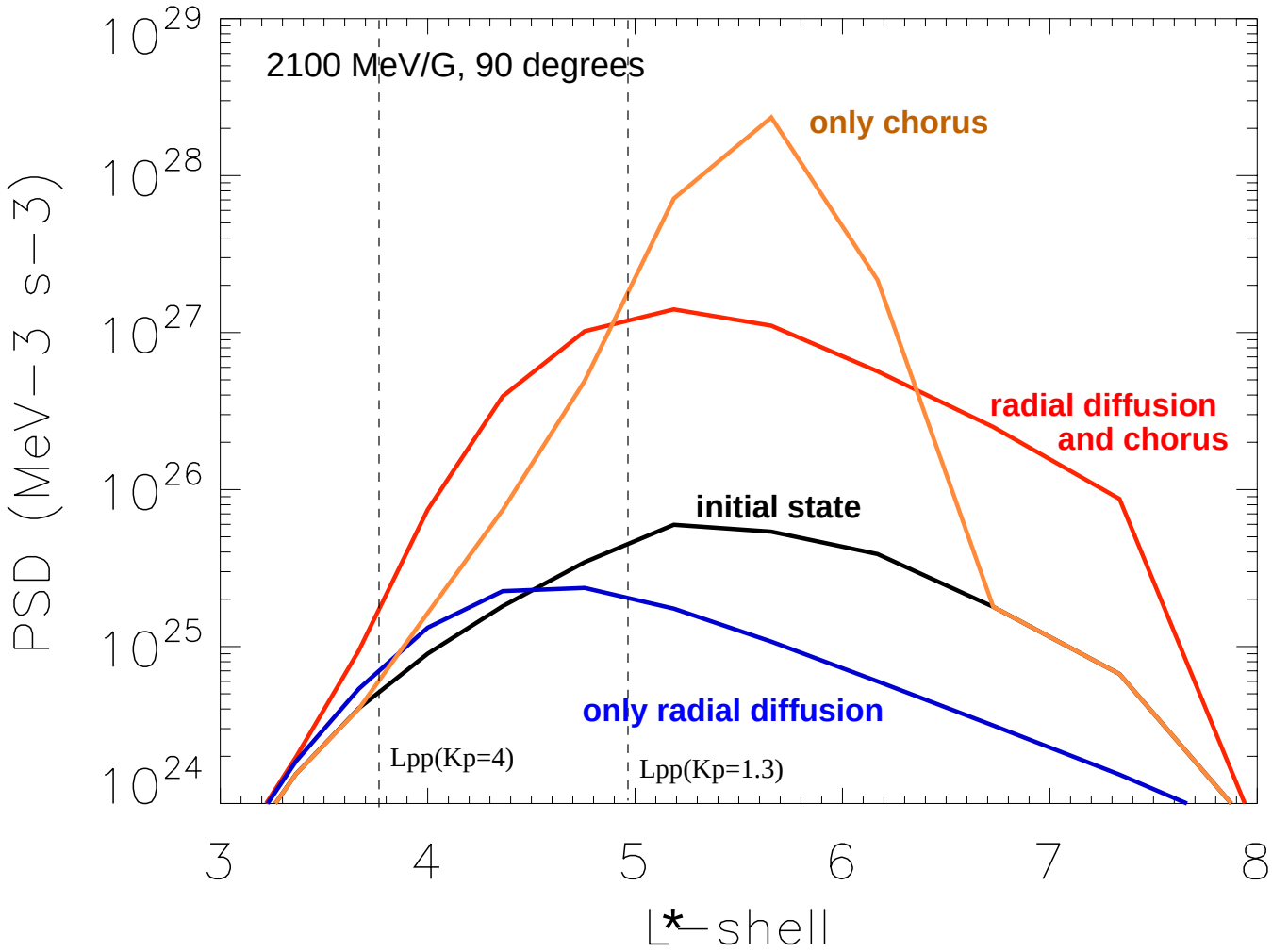

Figure 7. Phase Space densities (in MeV−3 s−3) for 2100 MeV/G equatorial particles as a function of L* from the three simulations at time T2: including only chorus wave interactions (orange line), including only radial diffusion (blue line) and including both processes (red line), starting from the same initial state (black line. Dashed lines show the position of the plasmapause for Kp = 1.3 and Kp = 4.

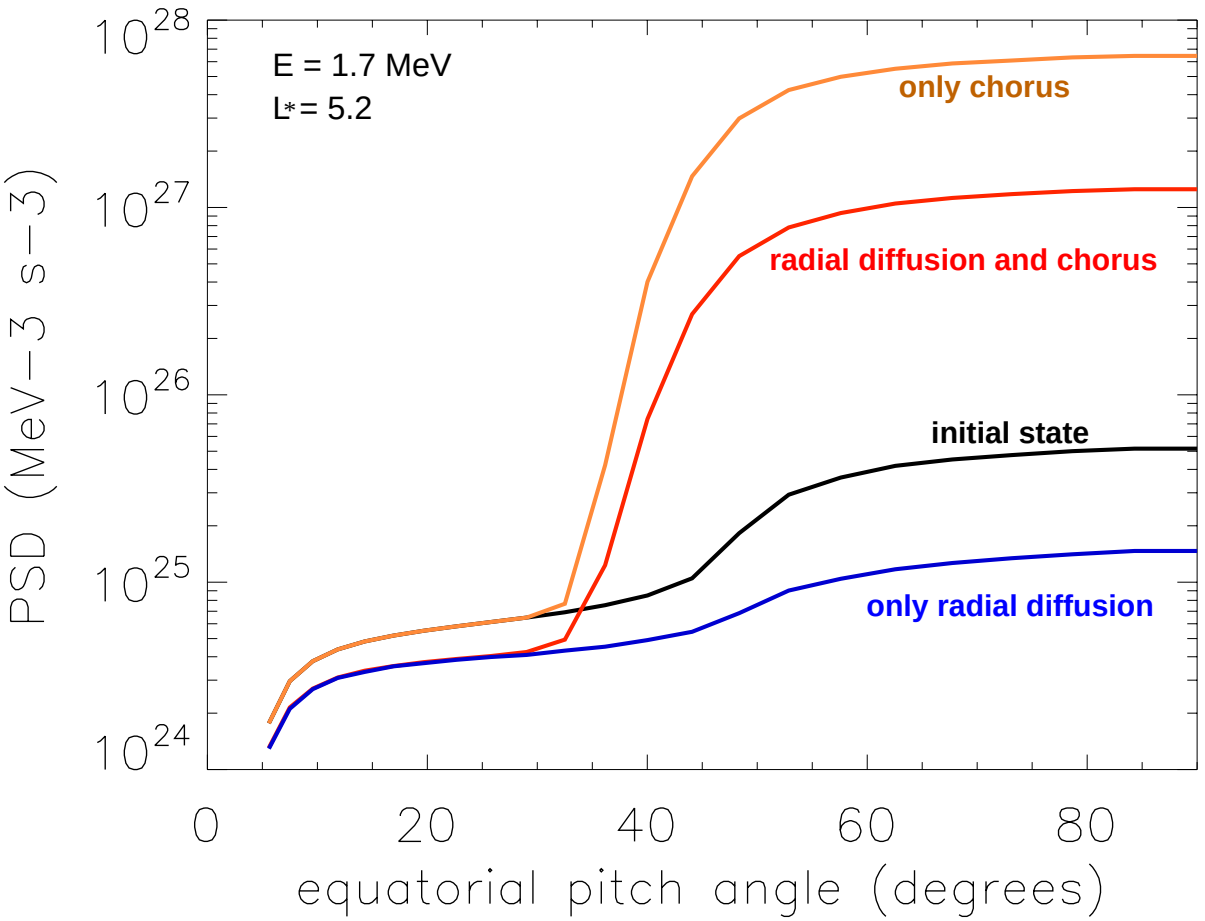

Figure 8. Phase space densities for 1.7 MeV electrons at L* = 5.2 as a function of equatorial pitch angle from the three simulations at time T2: including only chorus wave interactions (orange line), including only radial diffusion (blue line) and including both processes (red line),starting from the same initial state (black line).

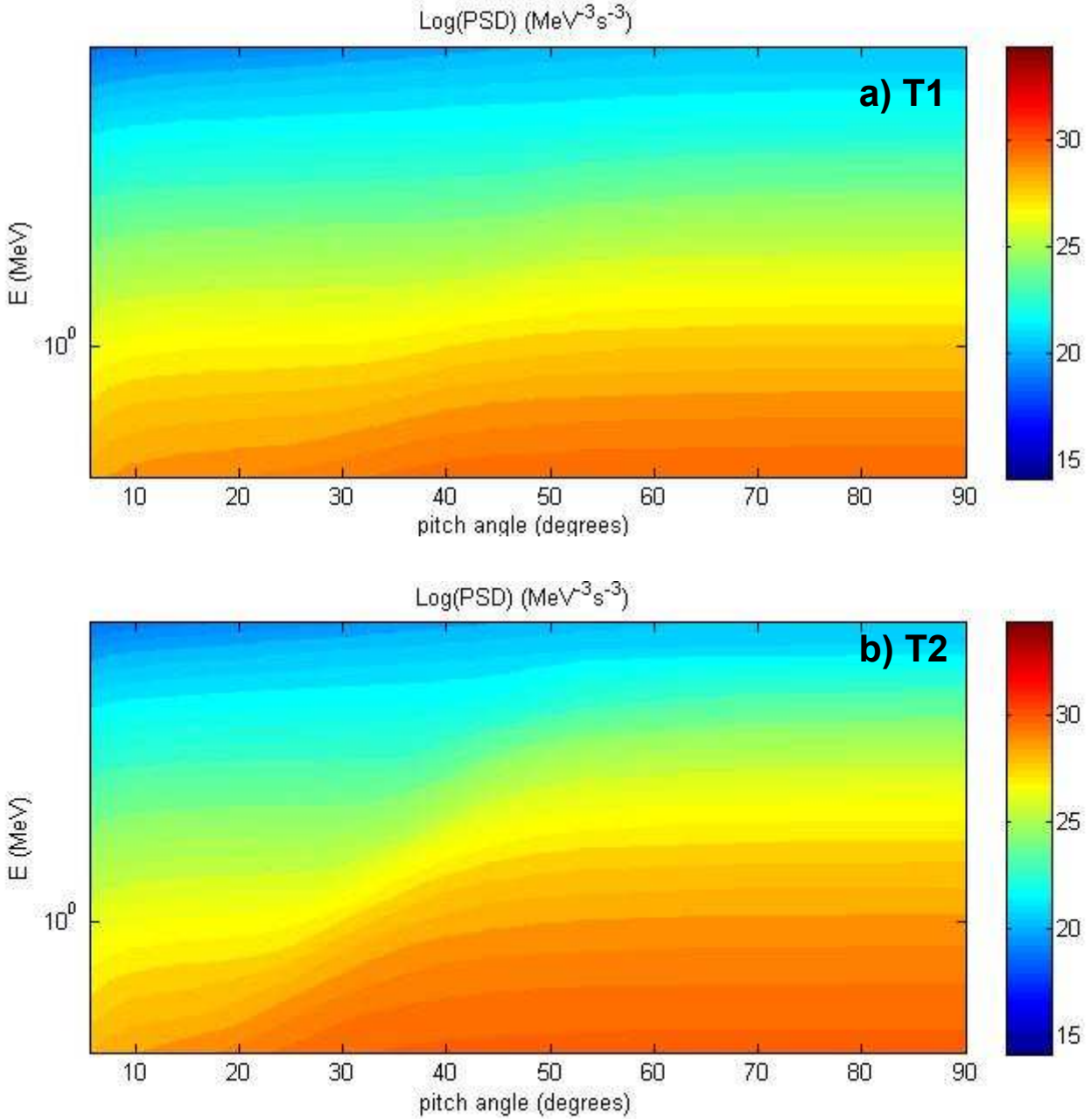

Figure 9. 2D plots of phase space densities at $L^* = 5.2$ as a function of energy (shown from 0.5 to 5 MeV on a log scale) and equatorial pitch angle at a) time T1 and b) time T2.

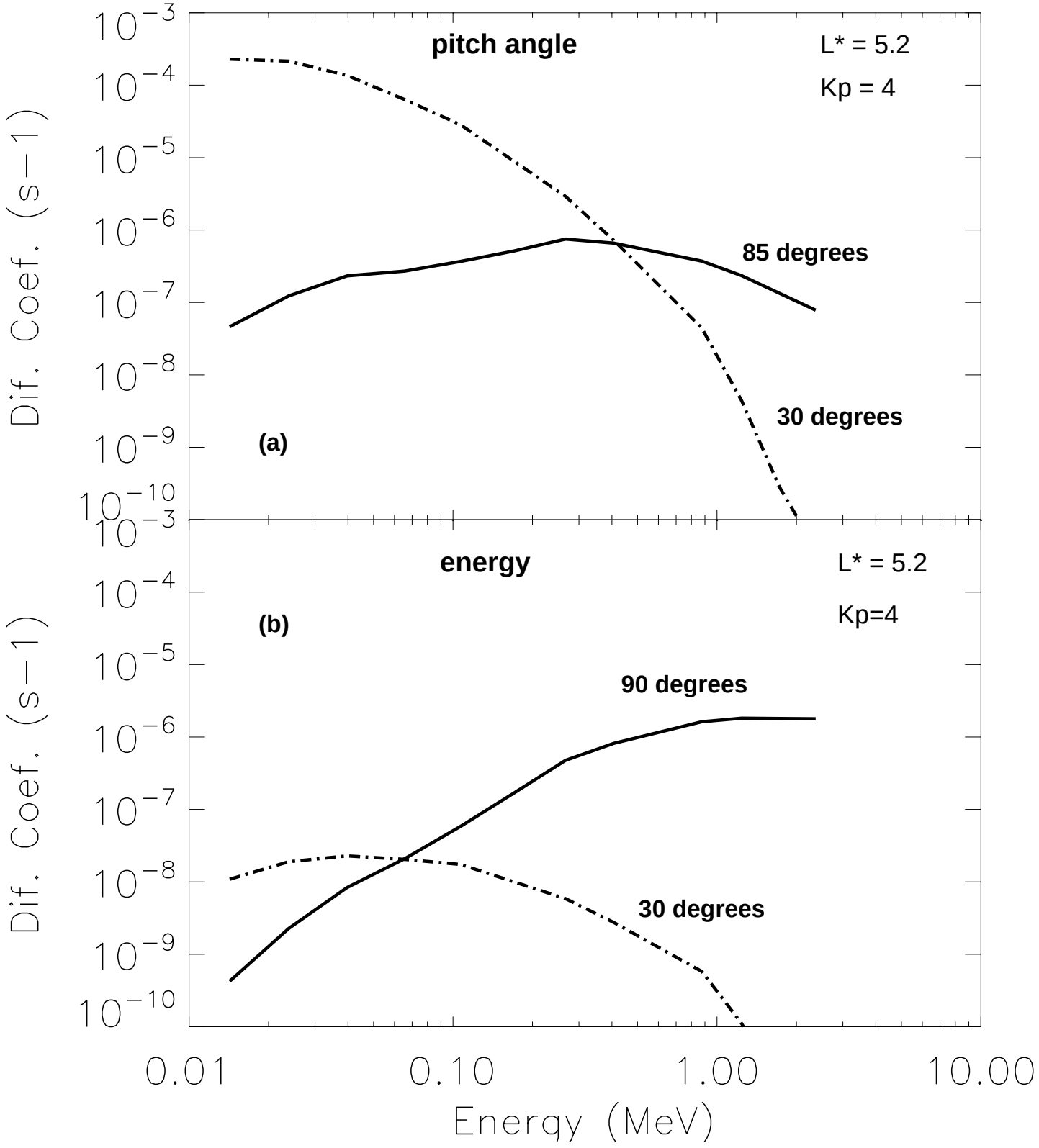

Figure 10. Diffusion coefficients as a function of energy for Kp = 4 and L* = 5.2: (a) pitch angle diffusion coefficients at 90 degrees (solid line) and 30 degrees (dash dot line) and (b) energy diffusion coefficients at 90 degrees (solid line) and 30 degrees (dash dot line).

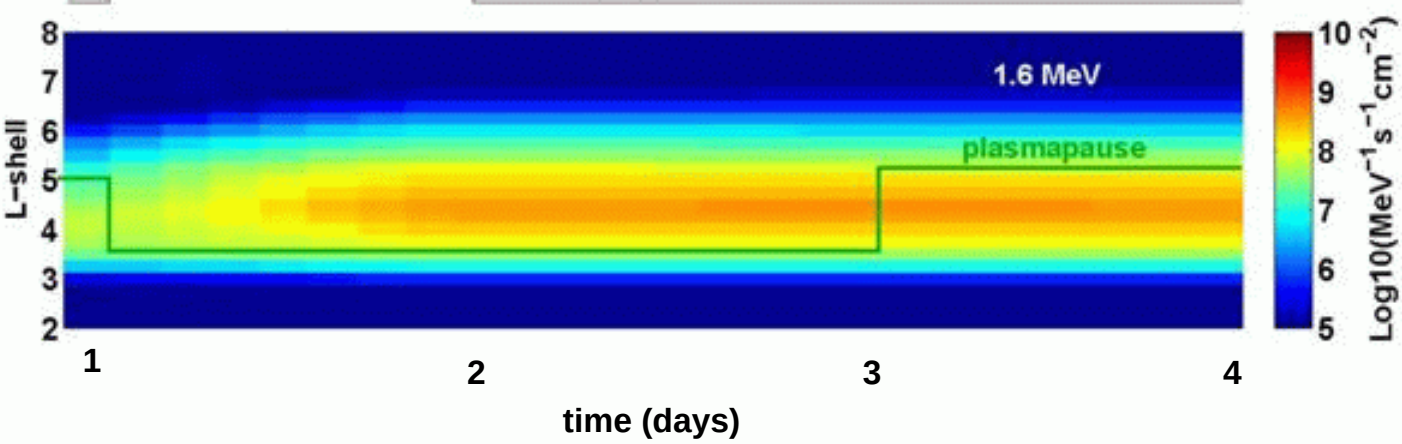

Figure 11. Omnidirectional equatorial flux variation during the test−case simulation for 1.6 MeV electrons. The plasmapause position is marked with a green line.

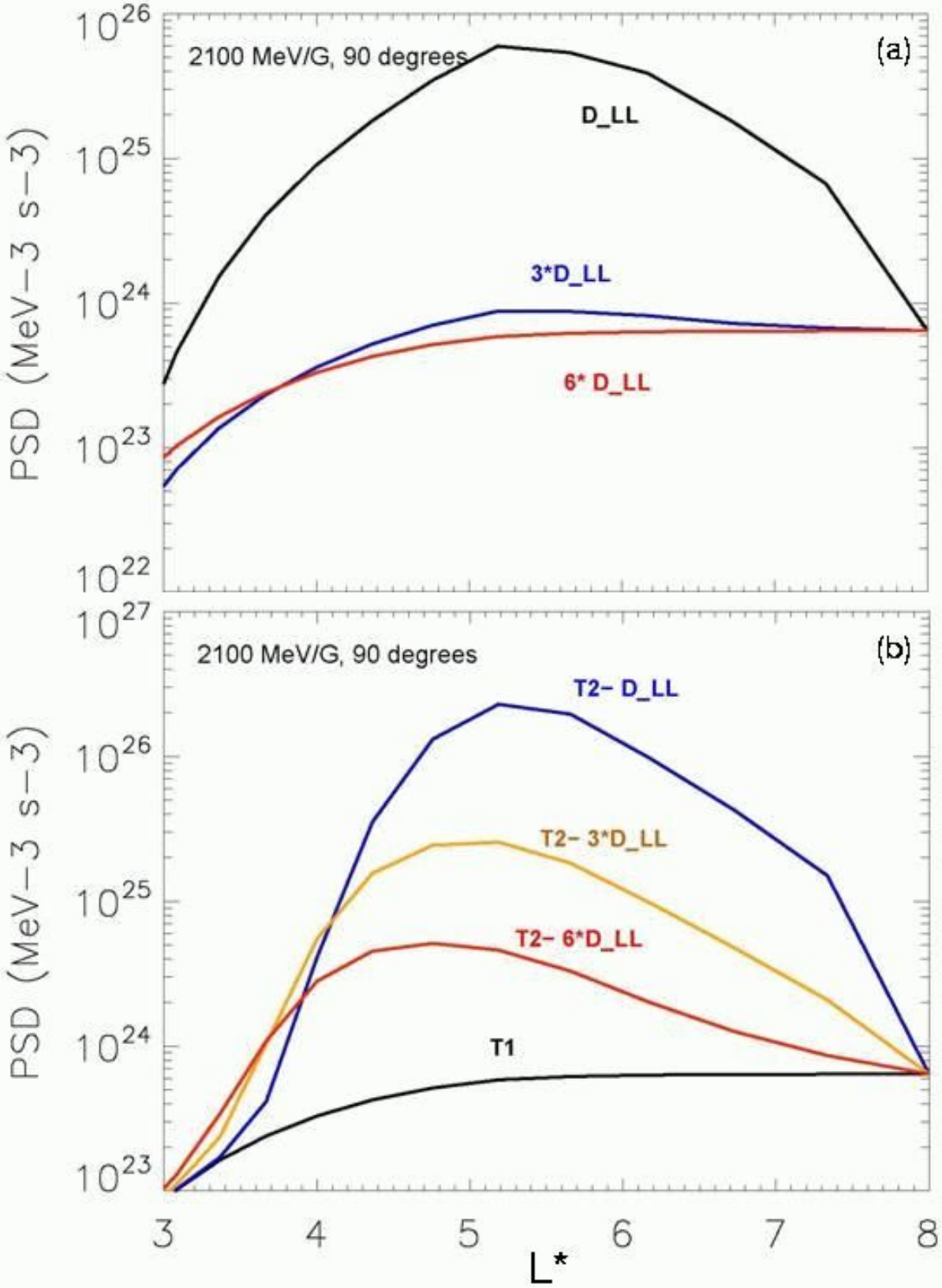

Figure 12. Phase space densities (in MeV−3s−3) for 2100 MeV/G equatorial particles as a function of L* for (a) the three steady state simulations and (b) at time T2 for the three dynamic simulations starting from the same initial state at T1.

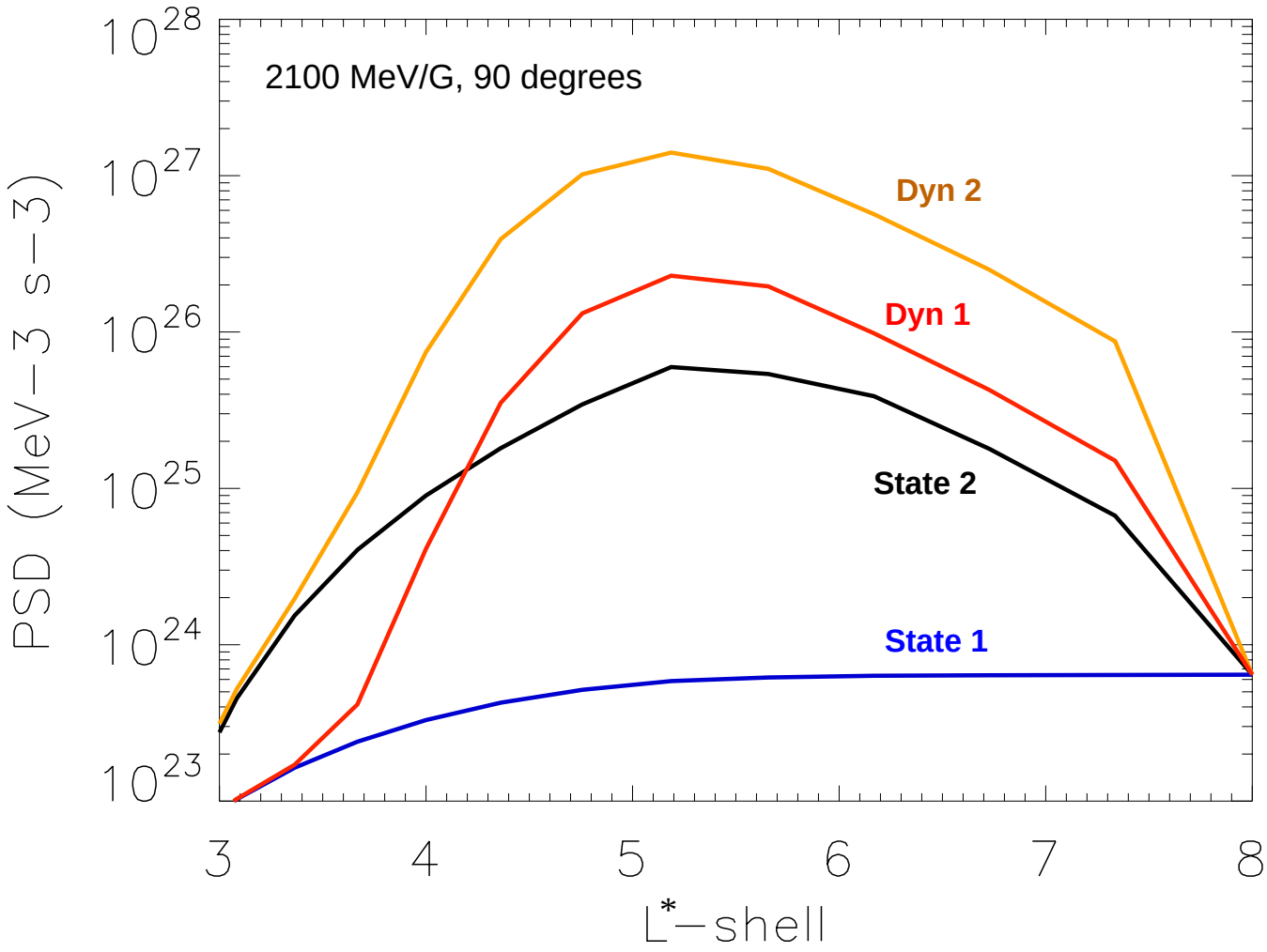

Figure 13. Phase space densities for 2100 meV/G equatorial particles as a function of L* at times T1 and T2 from two dynamic simulations: one starting from State 1 and one starting from State 2.

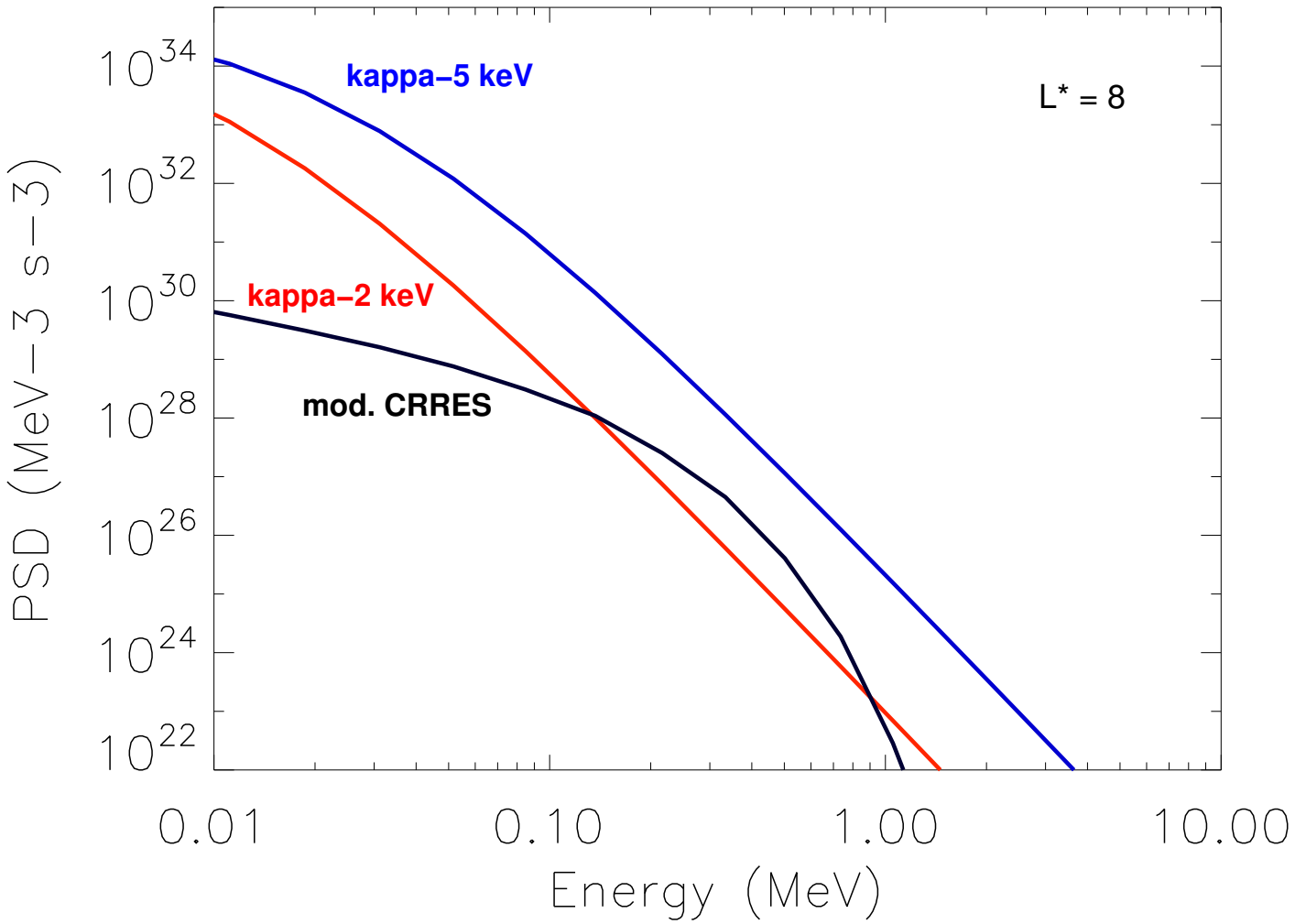

Figure 14. Spectrum of the three distributions used as a source at the outer boundary (L* = 8): the kappa distribution with Eo = 2 keV (red), the kappa distribution with Eo = 5 keV (blue) and the distribution taken from CRRES (black).

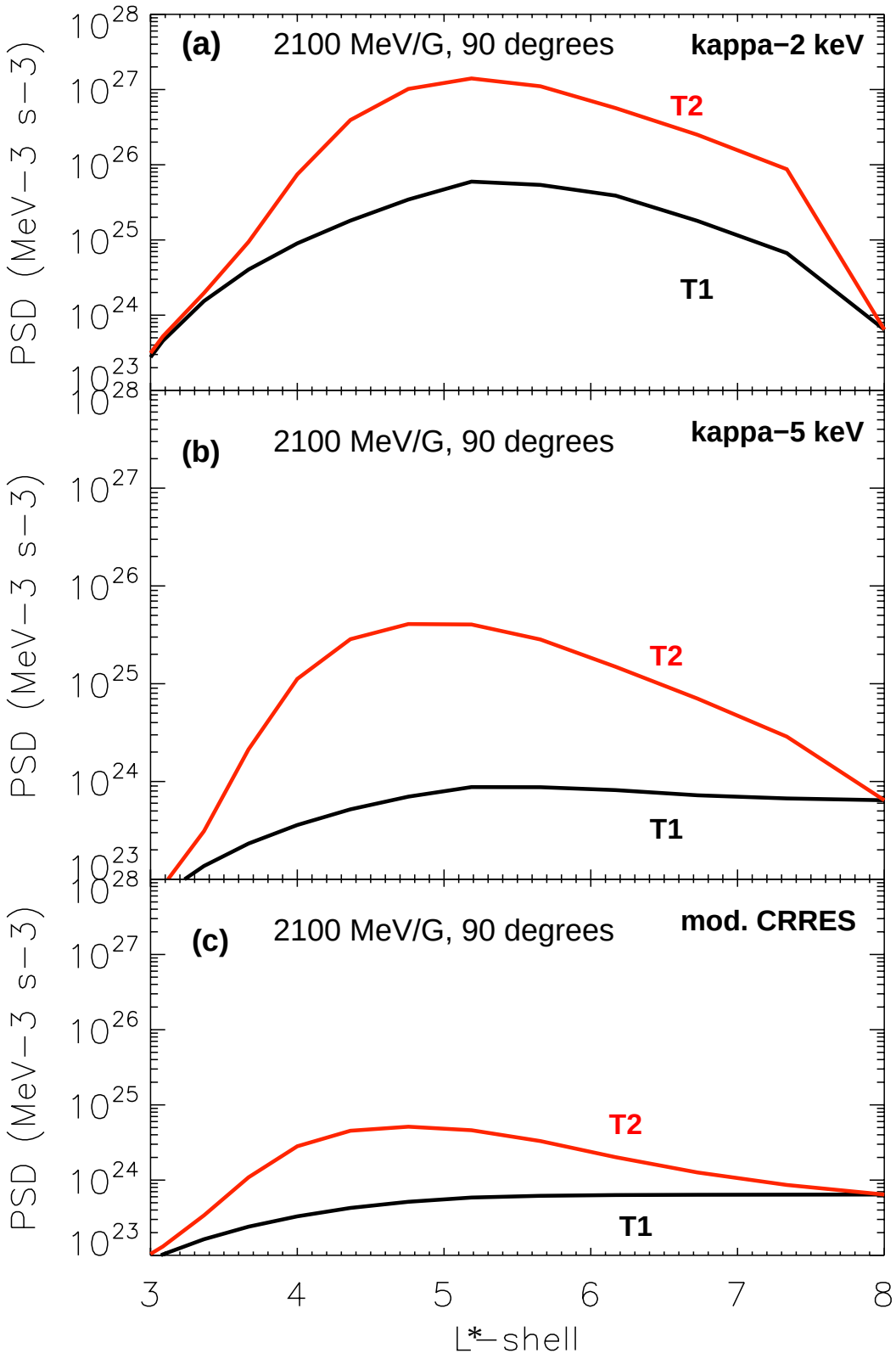

Figure 15. Phase space densities for 2100 MeV/G equatorial particles as a function of L* at times T1 and T2 using the three boundary conditions (a) a kappa distribution with Eo = 2 keV, (b) the kappa distribution with Eo = 5 keV and (c) the distribution taken from CRRES.